AGU100 ADVANCING EARTH AND SPACE SCIENCE

# JGR Earth Surface

**Key Points:**
- Coupled fluid-particle simulations provide micromechanical evidence to the pore pressure feedback mechanism in immersed granular collapses
- Large enough loose columns may liquefy to a rapid collapse that leads to hydroplaning during propagation, thereby enhancing the final runout
- A robust linear correlation exists between the runout distance and the densimetric Froude number regardless of the packing density and the problem scale

**Supporting Information:**
- Supporting Information S1
- Movie S1
- Movie S2
- Movie S3
- Movie S4
- Movie S5
- Movie S6
- Movie S7
- Movie S8
- Movie S9
- Movie S10

**Correspondence to:**
C. Y. Kwok,
fkwok8@hku.hk

# Pore-Scale Simulation of Immersed Granular Collapse: Implications to Submarine Landslides

**G. C. Yang[1], L. Jing[1,2], C. Y. Kwok[1], and Y. D. Sobral[3]**

[1]Department of Civil Engineering, The University of Hong Kong, Pokfulam, Hong Kong, [2]Now at Department of Chemical and Biological Engineering, Northwestern University, Evanston, IL, 60208, USA, [3]Departamento de Matemática, Universidade de Brasília, Campus Universitário Darcy Ribeiro, 70910-900, Brasília, Brazil

**Abstract** The collapse of granular columns in a viscous fluid is a common model case for submarine geophysical flows. In immersed granular collapses, dense packings result in slow dynamics and short runout distances, while loose packings are associated with fast dynamics and long runout distances. However, the underlying mechanisms of the collapse initiation and runout, particularly regarding the complex fluid-particle interactions at the pore scale, are yet to be fully understood. In this study, a three-dimensional approach coupling the lattice Boltzmann method and the discrete element method is adopted to investigate the influence of packing density on the collapsing dynamics. As a supplement to previous experimental measurements, the direct numerical simulation of fluid-particle interactions explicitly provides micromechanical evidence of the pore pressure feedback mechanism. In dense cases, a strong arborescent contact force network can form to prevent particles from sliding, resulting in a creeping failure behavior. In contrast, the granular phase is liquefied substantially in loose cases, leading to a rapid and catastrophic failure. This opposing dilative/contractive behavior linked to the initial packing is robust and does not depend on the column size. Furthermore, hydroplaning can take place in large enough loose cases due to the fast-moving surge front, which reduces the frictional resistance dramatically and thereby results in a long runout distance. More quantitatively, we are able to linearly correlate the normalized runout distance and the densimetric Froude number across a wide range of length scales, including small-scale numerical/experimental data and large-scale field data.

## 1. Introduction

Submarine landslide is one of the common natural disasters, which can be triggered by earthquakes, deposition of sediments, storm waves, volcanic island growth (Hampton et al., 1996; Locat and Lee, 2002; Masson et al., 2006), or even the release of methane hydrate (Nisbet and Piper, 1998). The primary hazards caused by submarine landslides include not only the direct destruction of infrastructures, such as communication cables, pipelines, and offshore drilling platforms but also the indirect damage by triggering giant tsunamis (Løvholt et al., 2017). Meanwhile, predicting the consequence of submarine landslides remains to be a challenge due to the lack of understanding of the flow dynamics, leading to difficulties in risk assessment and mitigation works.

A unique feature of submarine landslides, compared to subaerial landslides, is their extensive runout even on extremely gentle slopes. As a typical example, the well-known Storegga Slide reached more than 400 km at maximum on a 1– 2° slope (De Blasio et al., 2005; Bryn et al., 2005; Issler et al., 2005; Haflidason et al., 2005). One may expect that landslides in deep oceans are less mobile compared to subaerial landslides as they are driven by the reduced gravity due to buoyancy and subjected to additional resistance in the form of viscous drag. However, it was evidenced via small-scale laboratory experiments and numerical simulations that the runout distance of granular materials in a fluid can be longer than that in the absence of fluid due to lubrication effects (Rondon et al., 2011; Topin et al., 2012). Once particles travel at high speed, a thin wedge of pressurized fluid can be trapped between the sliding solids and the bed, significantly reducing the apparent bed friction and thereby increasing the mobility and producing long runout distance beyond expectation (Mohrig et al., 1998; Mohrig et al., 1999; Harbitz et al., 2003; Ilstad et al., 2004; De Blasio et al., 2004). It is worth mentioning that such simplified experiments and simulations may differ significantly from the settings in real landslides, such as material type and composition, but they are carefully designed to provide physical insights into field observations at least in a certain aspect of the whole complex process (Delannay et al., 2017).

On the other hand, the speed of friction dominated gravitational flows is found to be heavily dependent on the initial packing density, according to the results from the large-scale debris flow flume tests (Iverson, 1997; Iverson et al., 2000). Based on critical-state soil mechanics, soils tend to approach a specific void ratio under shear deformation (Wood, 1991). Densely packed soils dilate, which produces negative excess pore fluid pressure. As a result, the frictional resistance increases due to the increased effective stress thereby slowing down the granular flow. In contrast, loosely packed soils contract, which produces positive excess pore fluid pressure. Consequently, the frictional resistance decreases due to the reduced effective stress thereby accelerating the granular flow. In the literature, the positive feedback between frictional strength reduction and soil contraction is well known as the "pore pressure feedback mechanism" (Iverson, 1997; Iverson et al., 2000; Iverson, 2005).

The dependence of runout behavior on the initial packing density manifests different failure mechanisms. Recently, Pailha et al. (2008) and Mutabaruka et al. (2014) studied the time it takes for the initiation of an immersed granular avalanche using experiments and numerical simulations. A layer of glass beads with various initial packing densities was prepared and quickly inclined to a specific angle. It was found that, after the inclination, the loosely packed glass beads immediately liquefy and rapidly flow (contractive behavior), while the densely packed glass beads only slowly creep (dilative behavior).

The above-mentioned studies suggest that the packing density of the slope materials plays a crucial role in the initiation and runout of immersed granular flows, such as submarine landslides. In practice, the packing condition of the slope materials can vary both spatially and temporally due to different degrees of consolidation. For instance, landslides at deep sea fans of high-latitude areas along the Svalbard-Barents Sea margin consist of underconsolidated soils due to extremely high sedimentation rates, which are much softer than the Storegga sediments (Issler et al., 2005; Dimakis et al., 2000).

This study addresses the relevant physical mechanisms involved in immersed granular flows. The collapse of a granular column in air and in a viscous fluid has been recognized as an important phenomenon to study transient granular dynamics and the complex fluid-particle interactions (Crosta et al., 2009; Langlois et al., 2015; Utili et al., 2015; Rondon et al., 2011; Topin et al., 2012; Kumar et al., 2017; Bougouin and Lacaze, 2018; Jing et al., 2018; Jing et al., 2019; Staron and Hinch, 2005). Although the geometry is somewhat simplified, an immersed granular collapse retains the substantial features of a real submarine landslide, including flow initiation, transport of mass, and formation of deposit. Besides, field materials may exhibit various constitutive relations, while the influence of the packing density is expected to be qualitatively similar as long as the same dilatancy law and pore pressure model are applicable (Iverson, 2005).

Rondon et al. (2011) experimentally revealed the vital role of the initial packing density by measuring the induced excess pore fluid pressure underneath the granular column. The experimental observation qualitatively agreed with the aforementioned "pore pressure feedback mechanism" (Rondon et al., 2011). However, due to the difficulties of measuring the pressure field instantaneously in the experiments, the questions whether the excess pore fluid pressure is indeed caused by the dilation and contraction of the granular column and how it contributes to the slow and fast collapse dynamics remain to be answered. To answer these questions, characterization of pore-scale quantities inside the flows, such as local porosity and excess pore pressure, and different runout behaviors resulting from various initial packing conditions is required, suggesting the need of high-resolution numerical simulations.

The dilative and contractive regimes of an immersed granular column collapse have been qualitatively captured by a two-fluid smoothed particle hydrodynamics model (Wang et al., 2017) and continuum simulations (Lee and Huang, 2018; Si et al., 2018; Baumgarten and Kamrin, 2019). The major drawback of these methods is the lack of a unified rheological model, especially for transient problems at large deformations. In this regard, recent advancements in $\mu(I)$ rheology (Lagrée et al., 2011; Baumgarten and Kamrin, 2019) and granular thermodynamics (Jiang and Liu, 2007; Song et al., 2014) have been recognized as potential solutions to a universal continuum framework for granular flows. Two-dimensional (2-D) simulations via the discrete element method (DEM) coupled with a fluid solver have also been conducted (Topin et al., 2012; Kumar et al., 2017). However, 2-D models sometimes lead to unrealistic physical insights and limited conclusions due to the restricted kinematics. Particularly, in the case of immersed granular flows, a 2-D configuration leads to a compromised computation of turbulence and unreliable pore pressures due to the zero permeability caused by the discontinuous pore space, both of which can affect the dynamics of the granular column collapse dramatically.

The major goal of this paper is to characterize pore-scale dynamics (e.g., porosity, pore pressure, and force chain) and explore the effects of initial conditions (packing density and column size) on initiation and runout of immerse granular collapses. We perform three-dimensional (3-D) coupled fluid-particle simulations, in which particle kinematics is tracked by DEM (Cundall and Strack, 1979), and fluid dynamics is solved by the lattice Boltzmann method (LBM) (Chen and Doolen, 1998). The rest of this paper is organized as follows: section 2 presents the LBM-DEM formulation, which is verified against a benchmark problem of flow through a periodic array of spheres. The model configuration for immersed granular collapse is also presented followed by the case plan. Section 3 first gives an overview of the granular collapse in dense and loose states and then a detailed discussion on the micromechanics of collapse initiation. Section 4 discusses the runout dynamics with dimensionless numbers that determine flow regimes. Section 5 highlights the practical implications of our results regarding collapse initiation time and runout scaling, together with the limitations of this study. Section 6 draws concluding remarks on the major significance of this work.

## 2. Modeling Approach

Over the past two decades, LBM has been developed to become an alternative fluid solver to the traditional computational fluid dynamics (CFD). Our recent work has applied LBM as the first attempt to study the effects of bed form roughness on the transport of sediments in a turbulent environment (Yang et al., 2018). When CFD is coupled with DEM, a predefined drag model is essential to calculate the hydrodynamic forces between fluid and particles (Jing et al., 2016a). The CFD-DEM technique has been used to study the influences of aspect ratio, particle size, and fluid viscosity on the behaviors of granular collapse (Jing et al., 2018; Jing et al., 2019). However, due to the averaging involved in CFD-DEM, it can only provide limited pore-scale information that prevents us to uncover the physical mechanisms behind the role of packing density. Instead, the fluid-particle interaction can be fully resolved in LBM-DEM based on the fundamental law of momentum conservation (Ladd, 1994; Aidun et al., 1998; Noble and Torczynski, 1998). Furthermore, LBM-DEM can offer extensive pore-scale information benefiting from its finer spatial resolution and accurate reconstruction of the actual fluid velocity and pressure fields. In the following, we first present the LBM-DEM formulation and a validation case, followed by the model configuration of the immersed granular collapse and the case plan.

### 2.1. LBM-DEM Formulation

In LBM, the evolution equation with a Bhatnagar–Gross–Krook approximation (Bhatnagar et al., 1954) can be written as

$$f_i \left( \mathbf{x} + \mathbf{c}_i \delta_t, t + \delta_t \right) - f_i \left( \mathbf{x}, t \right) = -\frac{1}{\tau} \left[ f_i \left( \mathbf{x}, t \right) - f_i^{eq} \left( \mathbf{x}, t \right) \right], \tag{1}$$

where the density distribution function $f_i$ is related to the number of molecules at time $t$ positioned at $\mathbf{x}$ moving with velocity $c_i$ along the $i$th direction at each lattice node. The time step and the relaxation time are denoted as $\delta_t$ and $\tau$, respectively. The relaxation time $\tau$ physically determines how fast the density distribution functions recover the equilibrium state, $f_i^{eq}$, which is adopted as a Maxwellian one (Qian et al., 1992). The right-hand side of equation (1) is called the collision operator. A 3-D lattice structure with 19 discrete velocities (denoted as D3Q19) is adopted for a balance between accuracy and efficiency.

Based on the conservation of mass and momentum, the macroscopic fluid density $\rho_f$ and velocity $\mathbf{u}_f$ can be easily reconstructed from the velocity moments of the density distribution functions.

$$\rho_f = \sum_{i=0}^{18} f_i, \tag{2}$$

$$\rho_f \mathbf{u}_f = \sum_{i=0}^{18} \mathbf{c}_i f_i. \tag{3}$$

The Navier–Stokes equations can be recovered from equation (1) via a multiscale (Chapman–Enskog) expansion (He and Luo, 1997), and a relationship between the relaxation time $\tau$, the LBM time step $\delta_t$, the lattice spacing (size of a fluid cell) $\delta_x$, and the kinematic fluid viscosity $\nu_f$ is obtained as

$$\nu_f = c_s^2 \left( \tau - \frac{1}{2} \right) \frac{\delta_x^2}{\delta_t}, \tag{4}$$

where $c_s$ is the speed of sound and equal to $1/\sqrt{3}$ in lattice units for the D3Q19 lattice arrangement. Rearranging equation (4), the fluid time step can be calculated based on the fluid viscosity, the predefined relaxation time, and the spatial resolution. The pressure $p$ is related to the fluid density by the equation of state (He and Luo, 1997).

$$p = c_s^2 \rho_f. \tag{5}$$

DEM is adopted to take care of the mechanics of solid particles (Cundall and Strack, 1979). The particle–particle collisions are resolved based on a spring-dashpot analogy with a simplified Hertz contact model from Di Renzo and Di Maio (2004).

The magnitudes of the interparticle normal ($\mathbf{F}^n$) and tangential ($\mathbf{F}^t$) contact forces can be calculated as

$$F^n = k_n \delta_n + c_n \Delta u_n, \tag{6}$$

$$F^t = \min \left( \left| \left| k_t \int_{t_{c,0}}^{t_c} \Delta u_t \mathrm{d}t + c_t \Delta u_t \right| \right|, \mu F^n \right), \tag{7}$$

where $k_n$ and $c_n$ are the stiffness and damping coefficient in the normal direction. The overlap and the relative normal velocity are denoted as $\delta_n$ and $\Delta u_n$, respectively. $k_t$ and $c_t$ are the stiffness and damping coefficient in the tangential direction, respectively, the relative tangential velocity is denoted as $\Delta u_t$, and $\mu$ is the smallest of the friction coefficients of the two particles in contact. The integral in equation (7) represents the elastic tangential deformation of the particle surface since contact from time $t_{c,0}$ to $t_c$. The magnitude of the tangential force is limited by the Coulomb friction $\mu F^n$, at which the two contacting particles start to slide against each other. The stiffness ($k_n$ and $k_t$) and damping coefficients ($c_n$ and $c_t$) are nonlinear functions of the overlap $\delta_n$ with constants depending on several measurable material properties, namely, Young's modulus $E$, Poisson's ratio $\nu$, coefficient of restitution $e$, the size and mass of two particles in contact (see Appendix C in Jing et al. (2019) for further details).

The coupling between LBM and DEM is achieved by the immersed moving boundary method, initially proposed by Noble and Torczynski (1998). The fundamental principle of the immersed moving boundary method is to introduce a new collision operator, which depends on the solid ratio $\varepsilon$ for a specific lattice cell. The solid ratio $\varepsilon$ is defined as the volume fraction covered by the solid particle, whose value is estimated by a cell decomposition method (Owen et al., 2011) and ranges between 0 (fluid cell) and 1 (solid cell). In this way, equation (1) can be rewritten as

$$f_i \left( \mathbf{x} + \mathbf{c}_i \delta_t, t + \delta_t \right) - f_i(\mathbf{x}, t) = -\frac{1}{\tau} (1 - B) \left[ f_i(\mathbf{x}, t) - f_i^{eq}(\mathbf{x}, t) \right] + B \Omega_i^s, \tag{8}$$

where $B$ is a weighting function of the solid ratio $\varepsilon$ and the relaxation time $\tau$ (Noble and Torczynski, 1998).

$$B(\varepsilon, \tau) = \frac{\varepsilon(\tau - 1/2)}{(1 - \varepsilon) + (\tau - 1/2)}, \tag{9}$$

and $\Omega_i^s$ is the collision operator for solid cells. To ensure the no-slip boundary condition between fluid and solid, $\Omega_i^s$ is written based on the principle of nonequilibrium bounce back (Zou and He, 1997).

$$\Omega_i^s = f_{-i}(\mathbf{x}, t) - f_{-i}^{eq}(\rho_f, \mathbf{u}_f) + f_i^{eq}(\rho_f, \mathbf{u}_s) - f_i(\mathbf{x}, t), \tag{10}$$

where $\mathbf{u}_s$ is the macroscopic solid velocity at the position of the lattice node $\mathbf{x}$. The subscript $-i$ denotes the opposite direction of $i$.

The hydrodynamic force $\mathbf{F}_k^f$ on the $k$th particle can be calculated by summing the momentum transfer along all directions (from 0 to 18) at all lattice cells covered by the solid particle (from 1 to $N_{sc}$), which gives

$$\mathbf{F}_k^f = \sum_{j=1}^{N_{sc}} B_j \sum_{i=0}^{18} \Omega_i^s \mathbf{c}_i. \tag{11}$$

The hydrodynamic torque $\mathbf{T}_k^f$ is the cross product of the force and the corresponding lever arm, which can be written as

$$\mathbf{T}_k^f = \sum_{j=1}^{N_{sc}} \left[ B_j(\mathbf{x}_j - \mathbf{x}_k) \times \sum_{i=0}^{18} \Omega_i^s \mathbf{c}_i \right], \tag{12}$$

where $\mathbf{x}_k$ is the center of mass of the solid particle, and $\mathbf{x}_j$ is the coordinates of the $j$th solid or partially saturated cell.

Considering gravity ($\mathbf{G}_k$), contact forces and torques ($\mathbf{F}_k^c = \mathbf{F}_k^n + \mathbf{F}_k^t$ and $\mathbf{T}_k^c$), and hydrodynamic forces and torques ($\mathbf{F}_k^f$ and $\mathbf{T}_k^f$), the linear and angular velocities of particles can be easily calculated according to the Newton's second law.

$$m_k \mathbf{a}_k = \mathbf{F}_k^c + \mathbf{F}_k^f + \mathbf{G}_k, \tag{13}$$

$$I_k \dot{\boldsymbol{\omega}}_k = \mathbf{T}_k^c + \mathbf{T}_k^f, \tag{14}$$

where $m_k$ and $I_k$ are the mass and moment of inertia of the particle, respectively. Its acceleration is $\mathbf{a}_k$, and the angular velocity is $\boldsymbol{\omega}_k$. By integration in time of equations (13) and (14) via the Verlet method (Verlet, 1967), the position and orientation of particles can be updated.

To synchronize the fluid and particle simulations, 100 subcycles of DEM calculation are conducted for every step of LBM calculation, so it gives

$$\Delta t = \frac{\delta_t}{100}, \tag{15}$$

where $\Delta t$ is the DEM time step. During the subcycling procedure, the hydrodynamic force $\mathbf{F}^f$ and torque $\mathbf{T}^f$ acting on the particles remain unchanged.

### 2.2. Validation of Viscous Drag

The coupled LBM-DEM scheme presented in section 2.1 has been validated against a series of benchmark problems, together with a direct comparison between numerical results and experimental measurements regarding the immersed granular collapse (Yang et al., 2019). It was found that at least 20 lattice cells per particle diameter should be adopted to keep the errors in hydrodynamic forces below 5%. In addition, a small relaxation time greater than the lower limit 0.5 (see equation (4) for the constraint on positive fluid viscosity) should be used to ensure a small compressibility error and to strengthen the degree of coupling between fluid and particles. To further test the performance of the numerical model for problems involving a wide range of granular packing densities, LBM-DEM simulations of a viscous fluid flowing through a 3-D periodic array of spherical particles are carried out.

In numerical simulations, only one cubic cell with size $L = 0.01$ m is considered (see the inset of Figure 1). Periodic boundaries are defined in all faces. The fluid field has zero velocity initially. A small pressure gradient $\Delta P = 10^{-5}$ Pa/m is applied to drive the flow from left to right, while the sphere is forced to be stationary in position and rotation. The fluid density is $\rho_f = 1{,}000$ kg/m$^3$, and the fluid dynamic viscosity is $\mu_f = 0.001$ Pa·s. The lattice spacing $\delta_x$ and the relaxation time $\tau$ are set to be 0.1 and 0.8 mm, respectively. All simulations are run until a steady state is achieved at which the bulk flow velocity becomes stable and is denoted as $U$.

When the Reynolds number is small and the flow is laminar, viscous forces dominate over inertial forces. According to the Stokes's law, the drag force ($F_D^S$) from an infinitely large fluid field acting on a single sphere is linearly proportional to the flow velocity, which can be calculated as (Batchelor, 2000)
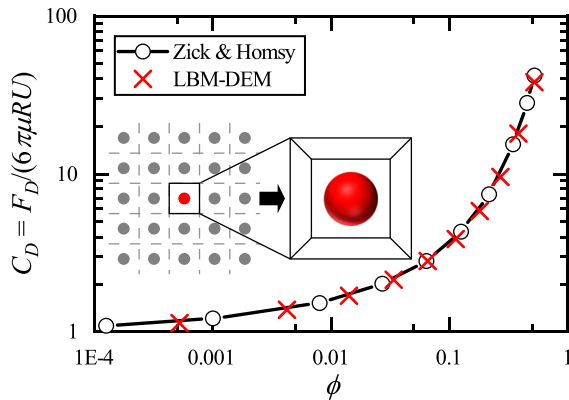
$$F_D^S = 6\pi\mu_f R U, \tag{16}$$

**Figure 1.** Comparison between lattice Boltzmann method-discrete element method (LBM-DEM) results and Zick and Homsy's solution for the drag coefficients $C_D$ for a wide range of solid fractions, $\phi$. The inset sketches a flow through an array of spheres. One cell is extracted and simulated using the LBM-DEM model with periodic boundary condition defined in all faces.

where $R$ is the radius of the spherical particle. Meanwhile, in the case of a periodic array of spheres, the fluid drag force is also a function of the packing density, $\phi = 4\pi R^3/(3L^3)$ (Zick and Homsy, 1982). A drag coefficient, $C_D$, can be defined as the ratio between the actual drag force on each individual sphere ($F_D$) and the Stokes drag $F_D^S$, that is, $C_D = F_D/F_D^S = F_D/(6\pi\mu_f RU)$. In this study, the particle radius $R$ is varied from 0.5 to 5 mm in order to calculate the drag coefficients for a wide range of packing densities.

Figure 1 compares $C_D$ between the LBM-DEM simulations and the analytical solution from Zick and Homsy (1982). It can be seen that $C_D$ increases dramatically as $\phi$ increases. The LBM-DEM results show an excellent agreement with the analytical solution over the entire range of packing densities. It means that the LBM-DEM algorithm presented in this work is capable of accurately describing the fluid-particle interactions for both densely and loosely packed systems, which serves as the cornerstone for studying the collapse of immersed granular columns with various initial packing densities.

### 2.3. Model Configuration

The coupled LBM-DEM method presented in section 2.1 and validated in section 2.2 is applied to simulate the immersed granular column collapse, as shown in Figure 2. The granular columns are composed of spherical particles of a mean diameter $d_p = 1$ mm with a weak polydispersity of 10% standard deviation following a Gaussian distribution. A layer of particles with a uniform size $d_p = 1$ mm is glued at the bottom to mimic a certain basal roughness (Jing et al., 2016b). The basal particles follow the simple cubic arrangement. All particles have an identical density $\rho_p = 2,500$ kg/m$^3$, close to that of soils and rocks. For particle–particle and particle–wall collisions, a Young's modulus $E$ and a Poisson's ratio $\nu$ equal to $10^9$ Pa and 0.24, respectively, are adopted. The coefficient of restitution is set to be $e = 0.65$. The coefficient of friction is $\mu = 0.4$. Both $e$ and $\mu$ are based on the property of quartz. The granular columns are fully immersed in a viscous fluid with a density $\rho_f = 1,000$ kg/m$^3$ and a dynamic viscosity $\mu_f = 0.01$ Pa·s. The initial height of the granular column is denoted as $H_i$. The horizontal and vertical spans of the simulation domain are set to be $l_x = 4H_i$ and $l_y = 1.5H_i$, respectively, which are large enough for the development of the final deposit with minimum boundary effects. Note that $l_x$ is extended to $6.25H_i$ in some large and loose cases to accommodate the longer runout distance. The periodic length in $z$ direction is fixed to be $l_z = 10d_p = 0.01$ m so that the finite-size effect is small. Simulations with a larger simulation domain of $l_z = 20d_p$ have been carried out, and no significant difference was observed.

The top surface is set to be a free-slip boundary condition, while no-slip boundary conditions are defined for the bottom wall and the side walls facing the $x$ direction. For the immersed cases, the lattice spacing $\delta_x$ and the relaxation time $\tau$ are set to be 0.05 mm (20 lattice cells per particle diameter) and 0.56, respectively,
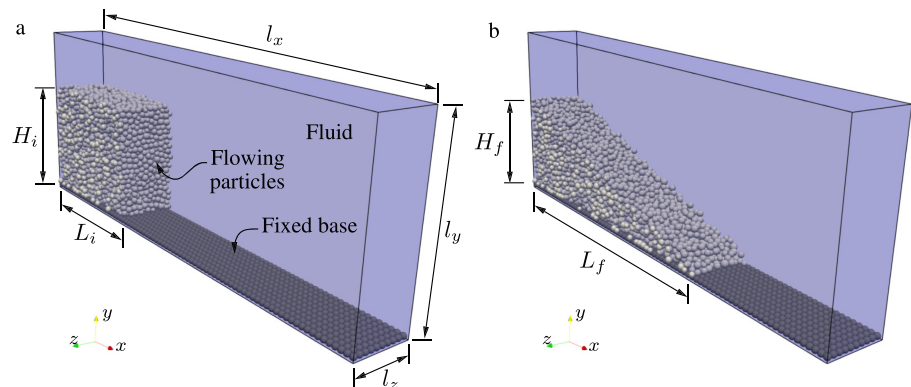


**Figure 2.** Model configuration of a granular column collapse in a viscous fluid: (a) initial condition and (b) final deposit ($H_i$ and $L_i$, initial height and length of the granular column, respectively; $l_x$, $l_y$, and $l_z$, length, height, and width of the simulation domain, respectively; and $H_f$ and $L_f$, height and length of the final deposit, respectively).

**Table 1**
*Case Summary of Lattice Boltzmann Method-Discrete Element Method Simulations. Only the Averaged Front Properties and the Averaged Dimensionless Numbers Governing the Flow Regimes are Presented. The Dimensionless Numbers are not Available for Flow Regime Analysis in the Dry Cases. See the Supporting Information for the Selected Video Animations*

| Series | Case label | $H_i$ (mm) | $L_i$ (mm) | $\phi_i$ (–) | $H_f$ (mm) | $L_f$ (mm) | $\tilde{L}_f$ (–) | $t_i$ (s) | $v_{ft}$ (mm/s) | $h_{ft}$ (mm) | $\dot{\gamma}$ (s$^{-1}$) | $\phi_{ft}$ (–) | $N_B$ (–) | $N_S$ (–) | $N_F$ (–) | $Fr_d$ (–) |
|---|---|---|---|---|---|---|---|---|---|---|---|---|---|---|---|---|
| Main immersed cases | D-S | 20 | 25 | 0.6277 | 20 | 49.5 | 0.98 | 0.265 | 37 | 3.15 | 11.6 | 0.454 | 2.44 | 0.019 | 136 | 0.170 |
| | M1-S | 20 | 25 | 0.5774 | 18 | 52.5 | 1.10 | 0.095 | 49 | 5.35 | 9.1 | 0.501 | 2.28 | 0.0067 | 354 | 0.173 |
| | M2-S | 20 | 25 | 0.5767 | 17 | 53.5 | 1.14 | 0.056 | 51 | 5.33 | 9.6 | 0.501 | 2.41 | 0.0075 | 336 | 0.182 |
| | L1-S | 20 | 25 | 0.5560 | 14 | 65.5 | 1.62 | 0.046 | 97 | 5.96 | 16.3 | 0.492 | 3.96 | 0.019 | 210 | 0.328 |
| | L2-S | 20 | 25 | 0.5502 | 13 | 70.5 | 1.82 | 0.046 | 106 | 5.96 | 17.9 | 0.482 | 4.16 | 0.023 | 185 | 0.359 |
| Dry counterparts | D-S-dry | 20 | 25 | 0.6277 | 19 | 57.5 | 1.30 | 0.011 | 246 | - | - | - | - | - | - | - |
| | M2-S-dry | 20 | 25 | 0.5774 | 18 | 57.5 | 1.30 | 0.007 | 214 | - | - | - | - | - | - | - |
| | L2-S-dry | 20 | 25 | 0.5501 | 17 | 58.5 | 1.34 | 0.015 | 210 | - | - | - | - | - | - | - |
| Different column sizes | D-VS | 16 | 20 | 0.6250 | 16 | 37.5 | 0.88 | 0.244 | 24 | 2.27 | 10.9 | 0.440 | 2.20 | 0.024 | 100 | 0.134 |
| | M1-VS | 16 | 20 | 0.5749 | 14 | 42.5 | 1.13 | 0.081 | 38 | 3.95 | 9.8 | 0.482 | 2.29 | 0.011 | 225 | 0.160 |
| | M2-VS | 16 | 20 | 0.5720 | 14 | 43.5 | 1.18 | 0.069 | 39 | 3.83 | 10.4 | 0.479 | 2.38 | 0.012 | 206 | 0.166 |
| | L-VS | 16 | 20 | 0.5524 | 12 | 49.5 | 1.48 | 0.045 | 79 | 5.05 | 15.7 | 0.485 | 3.71 | 0.021 | 182 | 0.289 |
| | D-B | 24 | 30 | 0.6296 | 23 | 62.5 | 1.08 | 0.285 | 57 | 4.61 | 12.5 | 0.470 | 2.80 | 0.015 | 198 | 0.219 |
| | M-B | 24 | 30 | 0.5789 | 20 | 67.5 | 1.25 | 0.088 | 61 | 5.17 | 12.2 | 0.507 | 3.17 | 0.014 | 273 | 0.225 |
| | L-B | 24 | 30 | 0.5506 | 14 | 91.5 | 2.05 | 0.047 | 112 | 6.61 | 17.0 | 0.479 | 3.95 | 0.019 | 211 | 0.359 |
| | D-VB | 32 | 40 | 0.6321 | 32 | 87.5 | 1.19 | 0.391 | 69 | 5.28 | 13.2 | 0.472 | 2.97 | 0.014 | 215 | 0.248 |
| | M-VB | 32 | 40 | 0.5789 | 26 | 98.5 | 1.46 | 0.075 | 101 | 8.50 | 12.0 | 0.520 | 3.24 | 0.0073 | 461 | 0.286 |
| | L-VB | 32 | 40 | 0.5501 | 17 | 148.5 | 2.71 | 0.048 | 172 | 8.83 | 19.5 | 0.485 | 4.62 | 0.019 | 253 | 0.477 |

which gives the LBM time step $\delta_t = 5 \times 10^{-6}$ s. Following equation (15), the calculated DEM time step is $\Delta t = 5 \times 10^{-8}$ s. Pure DEM simulations of the dry counterparts of the selected immersed cases are also conducted with a smaller time step $\Delta t = 10^{-8}$ s to ensure numerical stability. To verify our numerical parameters, higher spatial (up to 25 lattice cells per particle diameter) and temporal (with $\tau$ as small as 0.53) resolutions for the immersed cases, together with a smaller DEM time step $\Delta t = 10^{-9}$ s for the dry cases have been tested. No observable difference could be identified. Note that the mean particle diameter in our simulations is around 4.5 times larger than that of the glass beads in Rondon et al. (2011). To simulate the experimental cases reported by Rondon et al. (2011) with the same resolution, the number of particles and fluid cells would be more than $10^5$ and $10^9$, respectively, which exceeds our available computing power (Yang et al., 2019). The effect of particle size on collapse dynamics is briefly discussed in section 5.2.

Granular columns are prepared via the following steps. First, particles with a reduced mean size equal to $0.5d_p$ are created in a space with $x \in (0.0, L_i)$, $y \in (0.0, l_y)$, and $z \in (0.0, l_z)$, where $L_i$ is the initial length of the granular column. The initial velocities of the particles are 0, and there is no initial contact among particles. A "virtual gate" facing the $x$ direction is positioned at $x = L_i$ to prevent the particles from escaping. All particles are then gradually enlarged until the targeting mean size $d_p$ is achieved. Second, a reduced gravitational acceleration $g(\rho_p\text{-}\rho_f)/\rho_p$, with $g = 9.81$ m/s$^2$, is applied to make the particles settle. During this precipitation stage, the friction coefficient $\mu$ and the rolling friction coefficient $\mu_r$ are varied from 0 to 1 to generate granular columns with different initial packing densities (see Table 1). The rolling resistance model applies a constant torque, proportional to the coefficient of rolling friction, against the relative rotation of two contact particles to mimic the shape effects (Ai et al., 2011). In general, granular columns generated with higher values of $\mu$ and $\mu_r$ have smaller packing densities.

Once all particles are well settled down and concentrated at the lower part of the simulation domain, the friction coefficient $\mu$ is adjusted back to 0.4, and the rolling friction is turned off. For the wet cases, gravity remains unchanged to account for the buoyancy effect, while for the dry cases, gravity is adjusted to $g$. Additional DEM cycles are performed until the total kinetic energy of the particles is negligible. After that, the particles located above $y = H_i$ are deleted so that granular columns with an initial aspect ratio equal to $H_i/L_i = 0.8$ are obtained. Thus, the granular collapses in this study are more relevant to shallow landslides,

in which the initial free fall of the materials is negligible (Jing et al., 2018). Again, the granular systems are cycled to an equilibrium state, at which the particle kinetic energy is negligible. Finally, the linear and angular velocities of all particles are set to be 0. An example of a granular column can be seen in Figure 2a.

In this study, the local packing density at time $t$, $\phi(t)$, is calculated as the averaged solid volume fraction within small square query windows in the $xy$ plane with a size equal to $d_p$, that is,

$$\phi(t) = \frac{\sum_{\alpha=1}^{d_p/\delta_x} \sum_{\beta=1}^{d_p/\delta_x} \sum_{\gamma=1}^{l_z/\delta_x} \varepsilon_{\alpha\beta\gamma}(t)}{\left(\frac{d_p}{\delta_x}\right)^2 \left(\frac{l_z}{\delta_x}\right)}, \tag{17}$$

where $\varepsilon$ is the solid ratio of the fluid cells and $\alpha$, $\beta$, and $\gamma$ are the spatial indices. The initial packing density $\phi_i$ is taken as the averaged nonzero $\phi(0)$ values.

The particles are released by removing the gate and then collapse onto the bottom plane and spread horizontally. All simulations last for at least 2.0 s at which particles almost stop moving with the overall particle kinetic energy $E_k < 2.5 \times 10^{-10}$ J in all cases. Figure 2b shows a typical deposit of the granular particles at the end of the simulation (final deposit). The residual height and final runout of the flowing particles are denoted as $H_f$ and $L_f$, respectively.

### 2.4. Case Plan

Granular columns with four different sizes are prepared, including $L_i = 20$ mm (very small), 25 mm (small), 30 mm (big), and 40 mm (very big), which are denoted by the symbols VS, S, B, and VB, respectively. The different column sizes allow us to test the relevance of our flow regime analysis and runout scaling across a range of length scales (see sections 4 and 5), although it should be noted that all the granular columns simulated by LBM-DEM are far smaller than fieldscale submarine landslides. For each column size, the initial packing density varies between 0.55 (loose state) and 0.64 (dense state). The dense, medium dense, and loose packing densities are denoted by the letters D, M, and L, respectively. Labels are assigned to each case in the form of "packing density"-"column size". Cases with the same column size and the same level of packing density are distinguished by the numbers. According to Courrech du Pont et al. (2003), the Stokes number and the density ratio for our immersed granular collapses are calculated to be 0.8 and 1.6, respectively, which determines a transitional regime where both the fluid viscous and inertial effects are significant (Bougouin and Lacaze, 2018; Jing et al., 2019).

Three dry counterparts with a small column size are performed for comparison (marked by "dry"). Note that pure DEM simulation is performed for the dry cases (granular column collapses in vacuum), in which the influence from the interstitial air is ignored. Thus all references to the fluid in this work specifically refer to the viscous liquid in immersed cases. As a result, there are 18 cases in total, as summarized in Table 1.

## 3. Numerical Results

According to the simulation results, there is no noticeable variation in the spanwise ($z$) direction, meaning that the granular column collapse can be treated as a 2-D problem. Therefore we limit ourselves to collecting data at the midplane in the $z$ direction. The purpose of this section is to show the influence of the initial packing density, $\phi_i$, on the collapse dynamics. For simplicity, we focus on three immersed cases (D-S, M2-S, and L2-S) and their dry counterparts (D-S-dry, M2-S-dry, and L2-S-dry) with similar $\phi_i$ values and the same column size.

### 3.1. Overview of Granular Collapses
### 3.1.1. Immersed Granular Collapses in Dense and Loose States

Figure 3 shows the time sequence of the collapsing particles in the case D-S, which are painted according to their displacements in the $xy$ plane ($\delta_{xy}$). At a short time $t = 0.05$ s after the gate removal, only a few particles at the top-right corner show a sign of movement. The whole granular column remains in a fairly rectangular shape even at $t = 0.1$ s. A small eddy starts to develop, rotating in the counterclockwise direction. After a period of delay, the collapse initiates with a vertical fall of particles at the top-right corner, which can be clearly seen at $t = 0.3$ s. This localized failure behavior qualitatively agrees with the experimental observations from Rondon et al. (2011). Along with the fall of particles, the induced eddy further grows into a larger
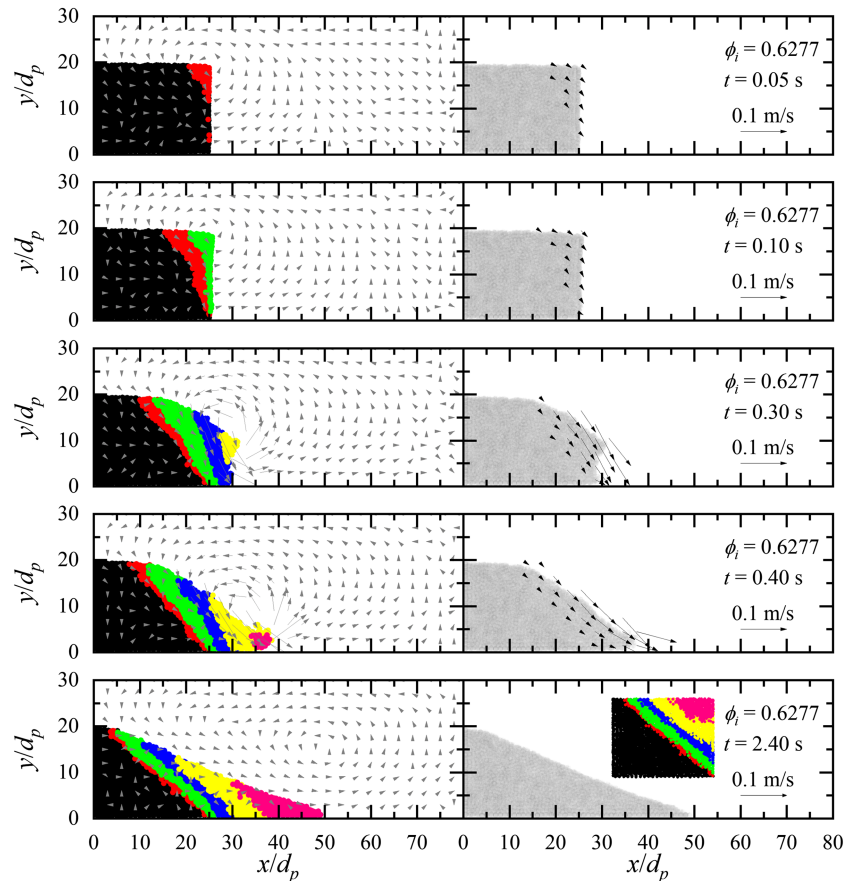
**Figure 3.** Case D-S. Left panel: snapshots of particles during the granular column collapse in a viscous fluid. The particles are painted according to their displacements in the $xy$ plane: black ($\delta_{xy} \leq 0.5d_p$); red ($0.5d_p < \delta_{xy} \leq d_p$); green ($d_p < \delta_{xy} \leq 5d_p$); blue ($5d_p < \delta_{xy} \leq 10d_p$); yellow ($10d_p \leq \delta_{xy} \leq 20d_p$); and pink ($\delta_{xy} > 20d_p$). The gray arrows indicate the magnitude and direction of fluid velocities. Right panel: the gray area shows the projection of the granular flow in the $xy$ plane. The black arrows indicate the magnitude and direction of particle velocities. Note that the particle velocities with magnitude smaller than 5 mm/s are not shown. The inset shows the painted particles at their initial positions.

size with much higher velocities. As the particles move towards the bottom plane, a high-pressure region is generated close to the toe of the granular column, which is evidenced by the suspended frontal particles at $t = 0.4$ s. Finally, the frontal particles spread horizontally with continuous sliding down of particles at the upper and steeper slope from $t = 0.4$ s to $t = 2.4$ s. The final granular deposit shows a trapezoidal shape with a small plateau on the left followed by a slightly concave slope on the right. The final height $H_f$ is close to the initial height $H_i$, that is, $H_f \approx H_i$.

Figure 4 shows the immersed granular column collapse in the case M2-S. In contrast to D-S, the failure of the medium dense case is initiated with the sliding of particles at the top-right corner along a shear plane going through the toe of the column (see Figure 4 for the particle velocity field at $t = 0.05$ s). The shear plane inclines roughly at 45° to the horizontal direction. An eddy is first generated due to the motion of particles at the top-right corner. As the particles keep sliding rightwards and downwards, from $t = 0.05$ s to $t = 0.1$ s, the eddy gradually grows into a size comparable to the initial column height $H_i$. It is the advancement of the granular front that mainly drives the fluid eddy at the beginning, then it is maintained by the sliding of particles at the surface of the granular flow and becomes less intensive at $t = 0.4$ s. At the later stage, the frontal particles propagate forwards in the horizontal direction and gradually decelerate. The final deposit shows a triangular shape with $H_f$ slightly smaller than $H_i$.

The failure of the loose granular column (L2-S) is regarded as catastrophic, as shown in Figure 5. Five unique features of the loose column collapse can be identified. First, once the gate is removed, the upper half of the column immediately falls down and drives the particles at the toe of the column rightwards. This is the
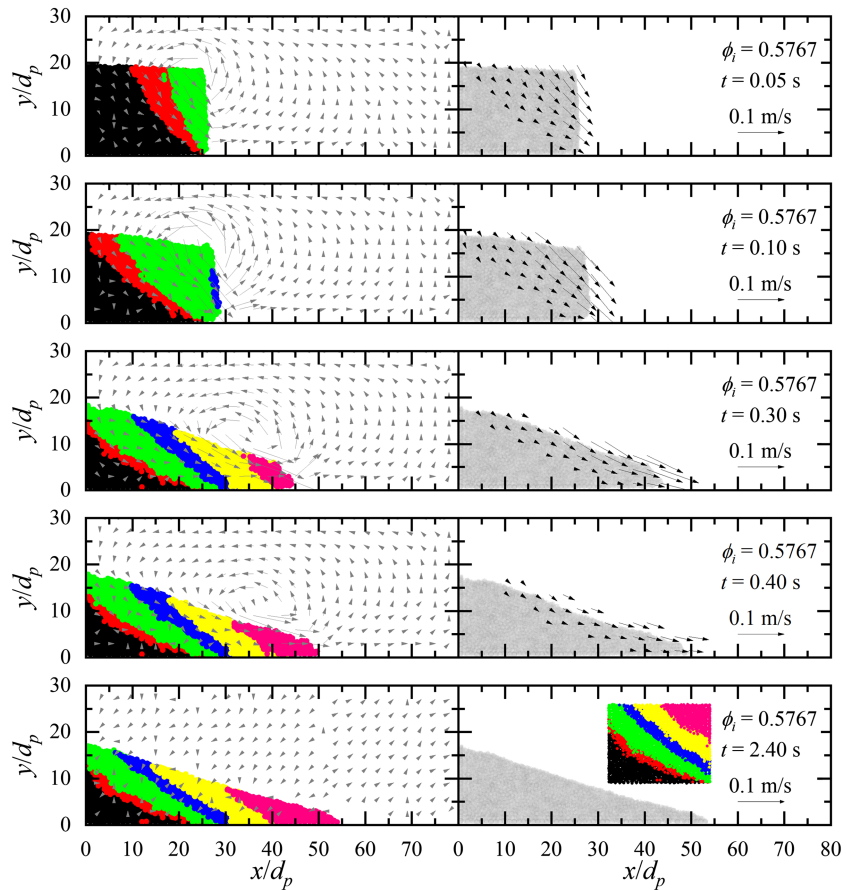
**Figure 4.** Case M2-S. See Figure 3 for the detailed caption.

cause of the concave interfaces in the particle displacement color map at $t = 0.05$ s. Second, from the particle velocity field, it can be seen that the loose column collapses at a much higher speed. As a result, a more intensive eddy is induced compared to those in D-S and M2-S. The high-intensity eddy generated in the loose case agrees with previous continuum simulations (Yu et al., 2018), implying that submarine landslides consisting of loosely packed soils might result in larger impulsive waves and become more tsunamigenic. Third, most of the particles in L2-S are mobilized during the collapse, with only a small portion at the left-bottom corner staying stationary ($\delta_{xy} \leq 0.5d_p$). In contrast, nearly half of the particles in D-S barely move during the whole collapsing period (see Figure 3). Fourth, the final deposit is more elongated and much thinner. Fifth, it can be seen that the surge front in the loose L2-S is composed of particles initially at the leading edge of the column. On the other hand, the particles initially at a much higher position fall down and become the major part of surge front in D-S (see the inserts of Figures 3 and 5). The residual height of the granular column is almost halved, that is, $H_f \approx 0.5H_i$.

There are two possible mechanisms for the formation of eddies. One is the momentum exchange between the viscous fluid and the solid particles, and the other is the mass displacement of grains. As the granular column collapses, the moving particles are able to set the surrounding fluid into motion through viscous drag. Theoretically, the fluid velocity is the same as the particle velocity (both magnitude and direction) at the solid lattice nodes due to the no-slip boundary condition imposed by equation (10). At the same time, the fluid also needs to fill the empty spaces left by the moving particles instantaneously so that the total mass (particles plus fluid) is conserved.

### 3.1.2. Evolution of Particle Kinetic Energy

Figure 6 compares the selected immersed cases to their dry counterparts regarding the time evolution of particle kinetic energy. The horizontal and vertical mean kinetic energies per grain, $\langle E_{kx} \rangle = \langle \frac{1}{2}mv_x^2 \rangle$ and $\langle E_{ky} \rangle = \langle \frac{1}{2}mv_y^2 \rangle$ are normalized by $mgd_p$ and denoted as $\langle \tilde{E}_{kx} \rangle$ and $\langle \tilde{E}_{ky} \rangle$, where $m$ is the mass of each individual particle, while $v_x$ and $v_y$ are the particle velocities in horizontal and vertical directions, respectively.
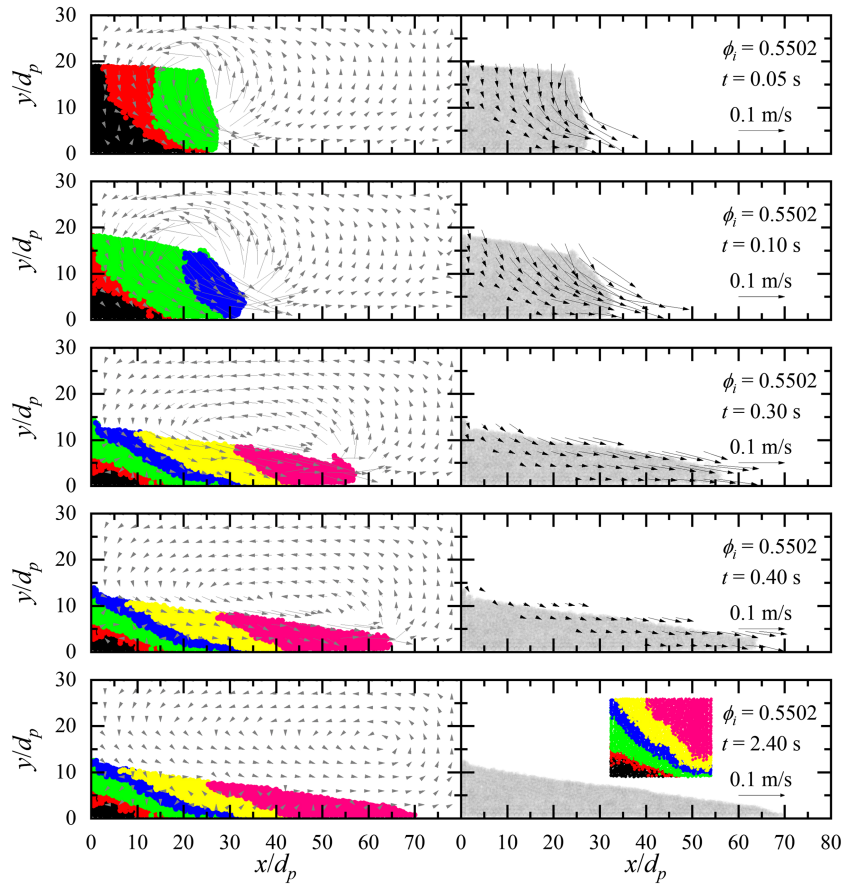
**Figure 5.** Case L2-S. See Figure 3 for the detailed caption.

First of all, despite the slightly fast development of the vertical kinetic energy in L2-S-dry, the overall collapse behavior in the dry cases is qualitatively the same regardless of $\phi_i$, as shown in Figures 6a and 6b.

However, Figures 6c and 6d reveal a significant role of $\phi_i$ on the collapse of granular columns in a viscous fluid. In D-S, there is negligible kinetic energy developed until 0.2 s after the gate removal. Then vertical fall of particles at the top-right corner takes place (see Figure 3), which is characterized by the growth of $\langle \tilde{E}_{ky} \rangle$ prior to $\langle \tilde{E}_{kx} \rangle$. In D-S, $\langle \tilde{E}_{ky} \rangle$ reaches the peak roughly at the time when the falling particles hit the bottom wall, between $t = 0.3$ and 0.4 s. The kinetic energy is gradually transferred from the vertical direction to the horizontal direction until the peak $\langle \tilde{E}_{kx} \rangle$ is reached at about $t = 0.4$ s. The peak $\langle \tilde{E}_{kx} \rangle$ and $\langle \tilde{E}_{ky} \rangle$ values in D-S are about the same at around 0.025. In contrast to D-S, $\langle \tilde{E}_{kx} \rangle$ and $\langle \tilde{E}_{ky} \rangle$ in both M2-S and L2-S start to increase immediately after the gate removal. In M2-S, $\langle \tilde{E}_{kx} \rangle$ grows together with $\langle \tilde{E}_{ky} \rangle$, which agrees with the sliding of particle along a 45° shear plane, as shown in Figure 4. The peak $\langle \tilde{E}_{kx} \rangle$ is noticeably higher than the peak $\langle \tilde{E}_{ky} \rangle$. In L2-S, the particle kinetic energy develops faster than that in D-S and M2-S. As the peak $\langle \tilde{E}_{ky} \rangle$ is reached at about $t = 0.1$ s, $\langle \tilde{E}_{kx} \rangle$ further develops to a significantly higher peak at about $t = 0.16$ s.

In the immersed cases, part of the particle kinetic energy is transferred to the fluid kinetic energy (see the eddies in Figures 3, 4, and 5) via fluid-particle interactions, leading to smaller peak $\langle \tilde{E}_{kx} \rangle$ and $\langle \tilde{E}_{ky} \rangle$ values compared to the dry cases. The particle kinetic energy gradually dissipates during the horizontal spreading period (after the peak) due to collision, friction, and viscous drag. A flow regime analysis to study the relative importance of various resistances to the stoppage of particles will be carried out in section 4.

### 3.1.3. Evolution of Runout Distance

Figure 7 shows the temporal evolution of the normalized runout distance, that is,

$$\tilde{L} = (L - L_i)/L_i, \tag{18}$$

where $L$ is the distance between the granular front and the left wall ($x = 0$). Due to the lack of fluid drag in the dry cases, their runout distances develop at a faster rate compared to that in the immersed cases. The
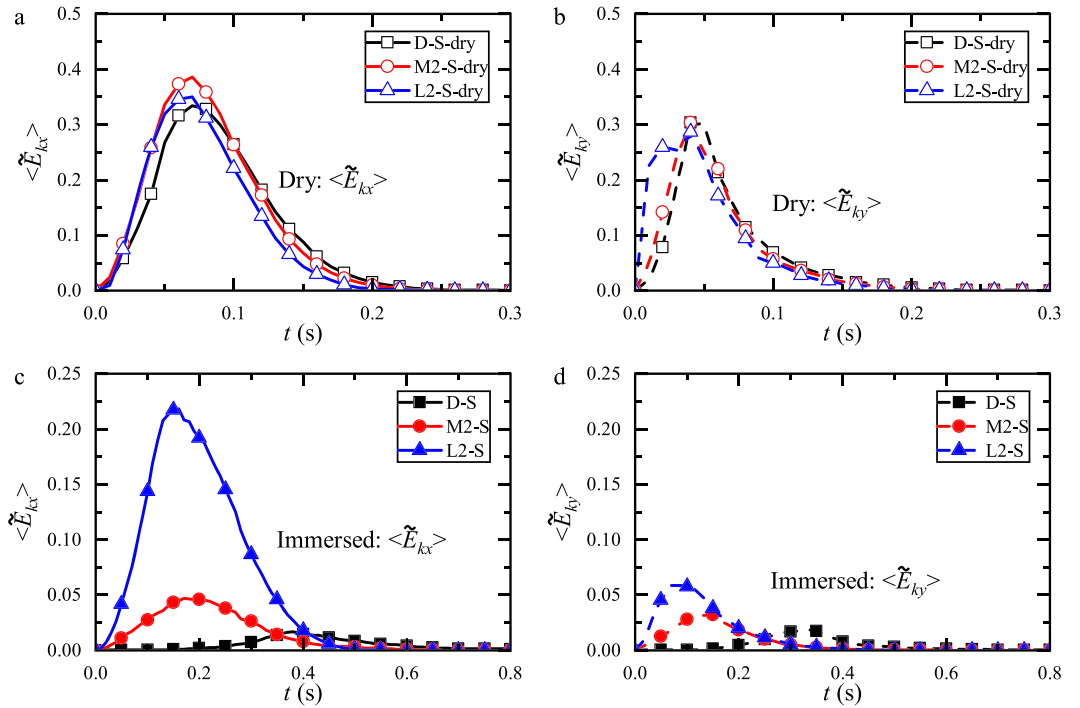
**Figure 6.** Evolution of the horizontal and vertical particle kinetic energies: (a) $\langle \tilde{E}_{kx} \rangle$ in the dry cases; (b) $\langle \tilde{E}_{ky} \rangle$ in the dry cases; (c) $\langle \tilde{E}_{kx} \rangle$ in the immersed cases; and (d) $\langle \tilde{E}_{ky} \rangle$ in the immersed cases. Note that the axis scales for (a, b) and (c, d) are different.

initial packing density of the granular column has a negligible effect on the runout behavior in the dry cases, which agrees with previous experimental results (Lajeunesse et al., 2005; Lube et al., 2005; Balmforth and Kerswell, 2005). However, in the immersed cases, the final normalized runout distance, $\tilde{L}_f$, is obviously a function of the initial packing density. $\tilde{L}_f$ is almost doubled as the granular column changes from a dense state (D-S) to a loose state (L2-S), although the total initial potential energy per particle is roughly equivalent in D-S and L2-S because of the same column size and shape. Besides, the larger acceleration of the immersed loose case is likely associated with a larger impulsive force on the fluid field, which may contribute to a more tsunamigenic scenario.

Direct evidence to the connection between the initial packing density and the initiation of immersed granular collapse will be provided in section 3.2 by examining the pore-scale (or particle-scale) properties. Furthermore, it is quite interesting to find in Figure 7 that L2-S produces a final runout distance much larger than that in the dry cases, even though the collapse in L2-S is driven by the reduced gravity due to buoyancy
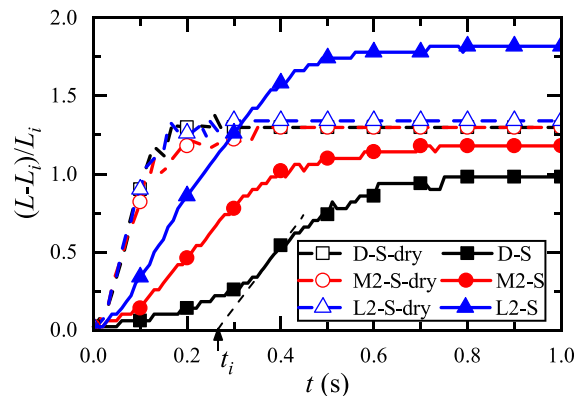


**Figure 7.** Comparison between the dry and immersed cases in terms of the time evolution of the normalized runout distance, $\tilde{L}$, in the dense, medium dense and loose states.
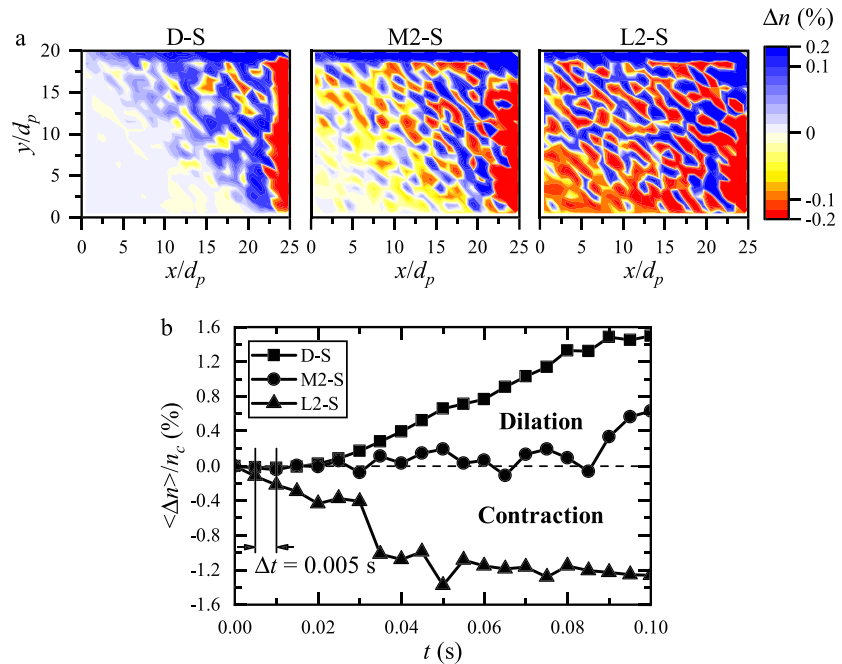
**Figure 8.** (a) Spatial distribution of the local porosity change $\Delta n$ during a short period from $t = 0.005$ to $0.01$ s in the selected immersed cases D-S, M2-S, and L2-S, respectively, from a dense state to a loose state; and (b) temporal evolution of the spatially averaged porosity change, $\langle \Delta n \rangle / n_c$, during the first 0.1 s. Positive value (increase of porosity) indicates dilation, while negative value (decrease of porosity) indicates contraction.

and suffers from additional resistance from the viscous drag. A possible mechanism for the different runout behaviors specifically depending on the initial packing density will be proposed in section 4.

### 3.2. Micromechanics of Collapse Initiation
### 3.2.1. Dilation and Contraction

First of all, we provide direct evidence of the dilation and contraction of the granular columns depending on their initial packing density $\phi_i$ by studying the change of local porosity $\Delta n$, where $n = 1 - \phi$. Figure 8a shows the spatial distribution of $\Delta n$ at the initiation stage from $t = 0.005$ to $0.01$ s, which are colored in a way that blue refers to positive $\Delta n$ (dilation) and red refers to negative $\Delta n$ (contraction).

First, we notice that the blue area on the top and the red area on the right are caused by the departure and approach of particles, respectively, due to the downward and forward movement under gravity. It is the local porosity change inside the granular column that shall be the indicator of dilation or contraction. A large blue area is observed in D-S, which means the particles need to climb over each other so that the collapse of the dense granular column can be initiated, resulting in a dilative behavior. As for M2-S, the red and blue areas are interlaced and roughly equally distributed inside the granular column. In this case, the local events of dilation and contraction are roughly balanced. However, in L2-S, the red area is noticeably larger than the blue area, indicating a predominantly contractive behavior.

To show the overall volume change of the granular columns, the evolution of the spatially averaged porosity change since the gate removal, $\langle \Delta n \rangle$, during the first 0.1 s is plotted in Figure 8b. $\langle \Delta n \rangle$ is normalized by a critical value $n_c = 0.42$, which is identified as a threshold between dilation and contraction from experimental observations (Rondon et al., 2011). Indeed, the direct simulation of particles in LBM-DEM shows that a dense column will dilate, and a loose column will contract during the collapse. It is expected that the degree of dilation and contraction during the initial acceleration phase will be dependent on the difference between the initial packing density ($\phi_i$) and its critical value 0.58.

On the other hand, it should be noted that the dilation and contraction of the granular skeleton only have a weak influence on the collapse dynamics in the dry cases, as shown in Figures 6 and 7. Therefore, the significant influence of dilation and contraction on the immersed granular collapse must come from the interstitial fluid.
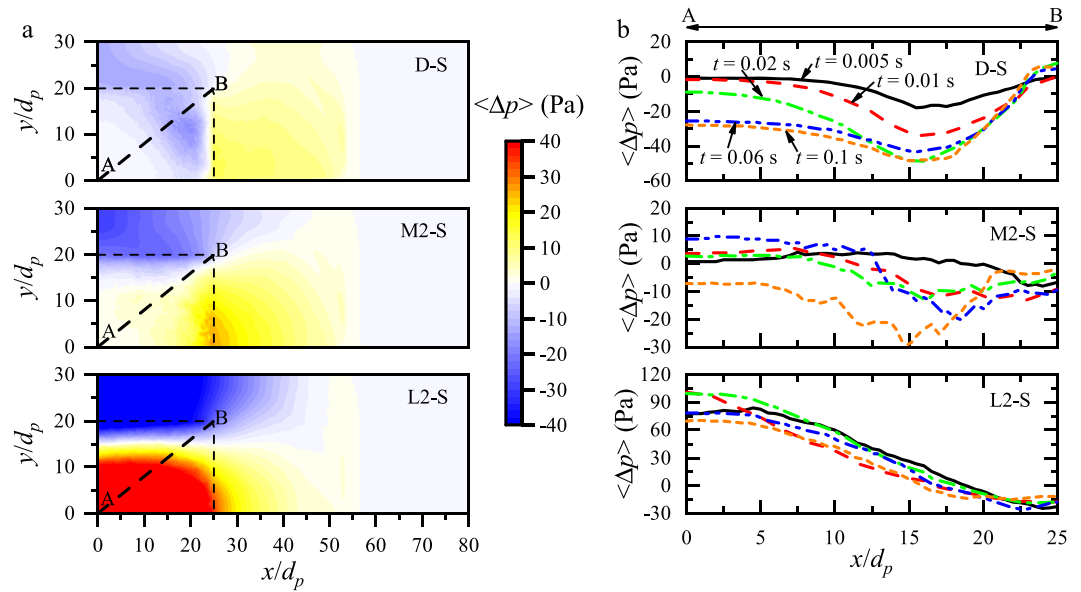
**Figure 9.** (a) Spatial distribution of the excess pore fluid pressure averaged in the $z$ direction, $\langle\Delta p\rangle$, at $t = 0.005$ s; and (b) spatial distribution of $\langle\Delta p\rangle$ along the diagonal line AB at $t = 0.005, 0.01, 0.02, 0.06,$ and $0.1$ s since the gate removal.

### 3.2.2. Excess Pore Fluid Pressure

Figure 9a shows the spatial distribution of the excess pore fluid pressure averaged along the $z$ direction, $\langle\Delta p\rangle$, just after the gate removal at $t = 0.005$ s for the selected immersed cases. The variations of $\langle\Delta p\rangle$ along the diagonal line AB are plotted in Figure 9b at $t = 0.005, 0.01, 0.02, 0.06,$ and $0.1$ s.

In D-S, a sequential development of negative $\langle\Delta p\rangle$ can be observed. The negative $\langle\Delta p\rangle$ is first induced close to the shear plane ($x/d_p \approx 17$) where sliding of particles starts initially (see Figure 3). Before $t = 0.01$ s, there is little $\langle\Delta p\rangle$ developed close to the left-bottom corner. As a result, a pressure gradient inside the granular column is generated, and the negative $\langle\Delta p\rangle$ gradually propagates from the shear plane to A until a limit state is reached at about $t = 0.06$ s. In M2-S, small positive $\langle\Delta p\rangle$ values are detected at $t = 0.005$ s, which means that limited contractions take place in M2-S at the beginning, probably due to its slightly larger initial porosity (0.4233) compared to $n_c$. As sliding occurs from $t = 0.005$ to $0.06$ s, positive $\langle\Delta p\rangle$ further develops close to the left-bottom corner ($x/d_p < 10$), while negative $\langle\Delta p\rangle$ is detected at $x/d_p > 10$ because of the low pressure zone left behind the flowing particles. From $t = 0.06$ to $0.1$ s, dilation dominates over contraction (also seen in Figure 8b), resulting in the sudden build up of negative $\langle\Delta p\rangle$ throughout the whole granular column. In contrast to D-S and M2-S, large positive $\langle\Delta p\rangle$ values are induced immediately after the gate removal in L2-S without any sequential development. The maximum positive $\langle\Delta p\rangle$ occurs close to the left bottom corner at around 90 Pa, which gradually decreases to $-30$ Pa from A to B.

### 3.2.3. Contact Force Characteristics

The induced excess pore fluid pressure has an impact on the particle–particle contacts and thereby affects particle resistance to sliding. Figure 10 shows the comparison of the contact force networks in the selected immersed granular columns. The magnitude of the contact force ($F_c$) is proportional to the thickness of the contact segments with their exact values indicated by the color bar.

As shown in Figures 10a–10c, the contact forces gradually increase as the depth increases in all cases due to the downward gravitational force. In D-S, before the gate removal, there are densely distributed particle–particle contacts inside the granular column. Once the gate is removed, as shown in Figure 10d, the dense granular column starts to collapse. The strong force chains tend to concentrate at the bottom-right corner and orient in a direction along with the sliding surface (see Figure 3). It is these strong force chains that support the whole granular column and prevent the particles from moving, resulting in the delay of collapse in the dense state. Localized initial fall of particles takes place at the most vulnerable top-right corner.

A similar evolution of the contact force network is also observed in cases M2-S and L2-S, except that the number of contacts is reduced as $\phi_i$ decreases. However, we do not observe an *arborescent* strong contact force network throughout the whole granular column after the gate removal in both M2-S and L2-S (see
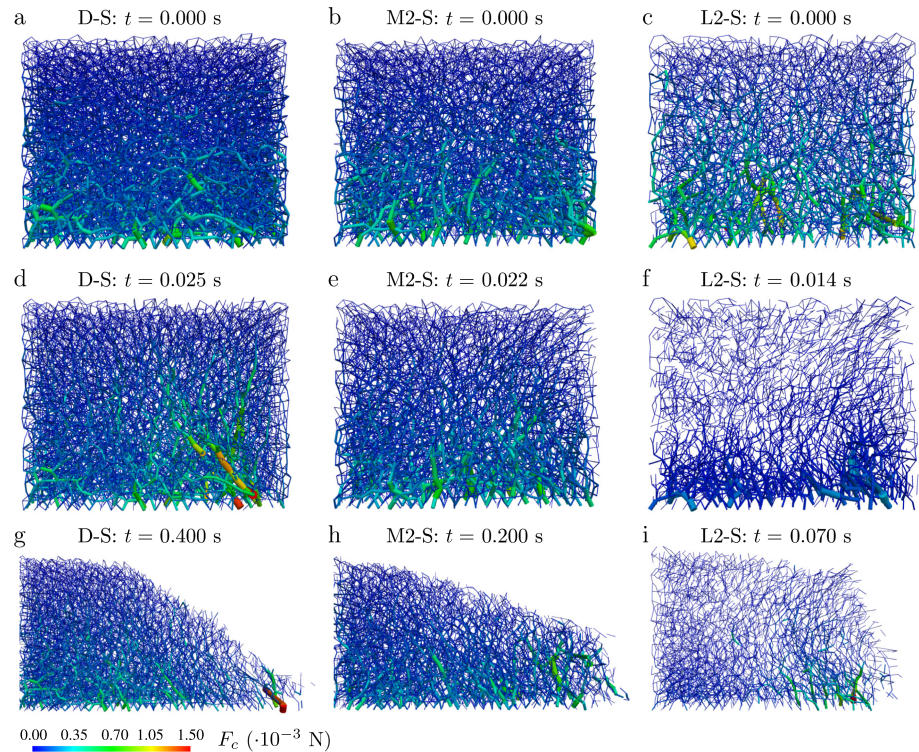
**Figure 10.** Comparison of the contact force networks in the immersed granular columns between D-S, M2-S, and L2-S: (a–c) before the gate removal at $t = 0$ s, (d–f) a short time after the gate removal, and (g–i) at a later stage when collapse has already taken place. The thickness and color of the contact segments denote the magnitude of the contact forces.

Figures 10e and 10f), which explains their immediate and fast collapse behaviors. Particularly in the case L2-S, most of the strong force chains disappear soon after the gate removal with only a limited amount of weak force chains remaining inside the granular column, which is attributed to the induced positive excess pore fluid pressure as shown in Figure 9. In other words, the particles are highly liquefied during the collapse in the loose state, and they behave like a "denser fluid" flowing in a "less dense fluid."

According to Radjaï et al. (1998), two sets of contact force networks exist in a granular assembly, including a strong one with $F_c > \bar{F}_c$ carrying the load and a weak one with $F_c < \bar{F}_c$ dissipating the energy via sliding, where $\bar{F}_c$ is the average contact force. However, in the granular collapse case, the strong force chains carrying the load (colored by yellow and red in Figure 10) have a magnitude much larger than the overall average contact force $\bar{F}_c$. In this study, in order to quantify these stronger force chains, the contact forces with a magnitude greater than three times of $\bar{F}_c$ are extracted and are denoted as $F_{cs}$. Figure 11 compares D-S, M2-S, and L2-S in terms of the angular distributions of these strong contact forces.

Let us first look at the change of contact force magnitude. Before the gate removal (see Figures 11a–11c), the strong contact force network in the dense D-S carries the least amount of average force, $\bar{F}_{cs}$, while the loose granular column (L2-S) has the maximum $\bar{F}_{cs}$ due to the much fewer particle–particle contacts (see Figure 10c). In D-S, $\bar{F}_{cs}$ increases during the initiation of the collapse (see Figure 11d) due to the induced negative excess pore fluid pressure (see Figure 9) from the dilation of the granular column (see Figure 8). At a later stage from $t = 0.025$ s to $t = 0.4$ s, $\bar{F}_{cs}$ decreases due to the dissipation of the negative excess pore fluid pressure. However, in M2-S, the variation of $\bar{F}_{cs}$ is small, as expected, since the induced excess pore fluid pressure is rather limited, as shown in Figure 9. In contrast to D-S, $\bar{F}_{cs}$ decreases significantly in L2-S from $t = 0$ to $0.014$ s because of the large positive excess pore fluid pressure, which gradually dissipates and hence later $\bar{F}_{cs}$ is more than doubled from $t = 0.014$ to $0.07$ s.

Apart from the contact force magnitude, the orientation of the contact forces also characterizes the different initiation behaviors in the dense and loose states. When the initial condition is considered at $t = 0$ s in D-S, the orientation of the contact forces is uniformly distributed from 0° to 180°. As the granular column becomes looser, the anisotropy of contact force orientation largely increases, as shown in Figures 11a–11c.
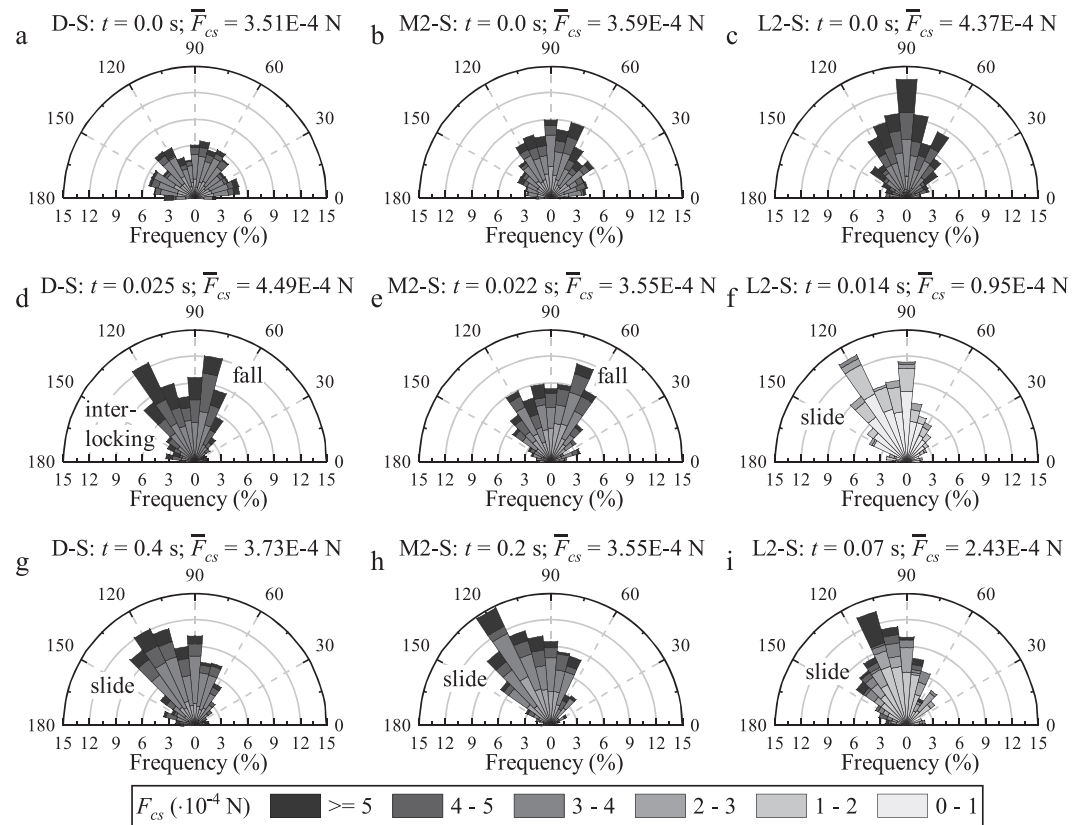
**Figure 11.** Angular distributions of the strong inter-particle contact forces for the cases D-S, M2-S and L2-S: (a–c) before the gate removal at $t = 0$ s, (d–f) a short time after the gate removal, and (g–i) at a later stage when collapse has already taken place. The color of each fan indicates the distribution of strong contact force magnitude, $F_{cs}$. Note that the selected time instances match with the moments when contact force networks are presented in Fig. 10.

Once the gate is removed, the contact forces rearrange themselves so that the ones close to the horizontal direction are significantly reduced in both D-S and M2-S due to the sudden loss of lateral support. In D-S at a short time after the gate removal, two preferential angles of contact forces can be identified: one is between 60° and 90° and the other is between 105° and 135° (see Figure 11d). The former is the clockwise rotation of contact forces mainly due to the fall of the top-right corner under gravity, which is also present in M2-S (see Figure 11e). The latter is caused by particle interlocking, which is absent in both M2-S and L2-S (see Figures 10e and 10f). At the later stage in Figures 11g–11i, all immersed cases approach a critical state in terms of the contact force orientation with only one preferential angle (the rose diagrams sway to the left), indicating a unified sliding behavior.

In summary, the increased $\bar{F}_{cs}$ in the dense case, or the increase of effective stress in the concept of soil mechanics (Wood, 1991), enhances the resistance of particles sliding against each other. It is the major reason for the delay of collapse and the slow dynamics observed in the dense state. The initial contact force network in the loose state shows a rather strong anisotropy in terms of the orientation. However, these strong force chains are vulnerable to buckling once the lateral prop is removed. Together with the weakened contact force network due to the induced positive excess pore fluid pressure, the catastrophic failure of the loose granular column becomes a matter of course.

## 4. Runout Dynamics

The large particle kinetic energy resulting from the catastrophic failure in the loose L2-S is apparently not the sole reason for its larger runout distance based on the fact that the dry counterparts have a larger particle kinetic energy, and yet their runout distances are relatively short (see Figure 7). This simple argument leads us to analyze the horizontal spreading (runout) stage in the immersed cases. We use dimensionless numbers to evaluate the flow regimes of the front propagation.
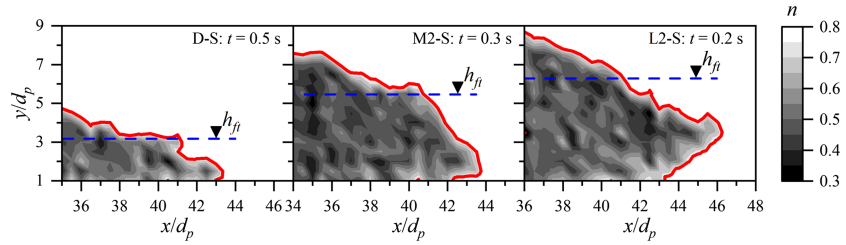
**Figure 12.** Comparison between D-S, M2-S, and L2-S in terms of the shape of the surge front, at typical time instances just after the occurrence of the peak $v_{ft}$. The surge fronts with $x > (L - 0.4L_i)$ are colored by the local porosity. A cutoff porosity equal to 0.8 is applied to separate the solid particles from the fluid field. The outline of the granular surge front is colored by the red solid line. The average thickness of the surge front is indicated by the blue dashed line.

### 4.1. Surge Front Properties

In this study, a particle is considered to be within the surge front if its $x$ coordinate is greater than $L - 0.4L_i$. The front velocity is calculated as the average horizontal velocity among all the particles forming the surge front. According to the time evolution of particle kinetic energy (see Figure 6), the particles quickly accelerate and then slowly decelerate after the initiation of collapse. The maximum front velocity during the entire simulation is extracted and denoted as $v_{ft}$.

A typical time when the surge front is propagating forward just after the occurrence of peak front velocity is considered. Figure 12 shows the spatial distributions of the local porosity at the front region in D-S, M2-S, and L2-S as $t = 0.5$, 0.3, and 0.2 s, respectively. A cutoff porosity ($n_{cut}$) equal to 0.8 is applied to separate the solid phase (gray) from the fluid phase (white). The fluid–solid interface is highlighted by the solid red line, which depicts the shape of surge front. The average thickness of the surge front, $h_{ft}$, can be calculated, which is marked by the blue dashed line in Figure 12. As the granular flow is spreading horizontally, the front thickness in D-S is only about half of that in cases M2-S and L2-S. In addition, a thin wedge of fluid is trapped underneath the granular front in M2-S, which is not observed in D-S at an initially dense state. Furthermore, this thin wedge of fluid becomes even more prominent in L2-S, which is powerful enough to lift up the surge front (hydroplaning; see section 4.2 for discussion).

### 4.2. Flow Regimes and Hydroplaning

As shown in Figure 12, the different dynamics of immersed granular collapses with various initial packing densities may result in a diversity of runout behaviors. The front velocity $v_{ft}$ and front thickness $h_{ft}$ can be strongly altered by the failure pattern. As a result, the relative importance between different sources of resistance, namely, collision, friction, and viscous drag, becomes entirely different, which has a direct impact on the stoppage of the surge front and thereby affecting the final runout distance $L_f$.

Dimensionless numbers have been proposed to weight these three resistances, referring to the Bagnold number $N_B$, the Savage number $N_S$, and the Friction number $N_F$ (Iverson, 1997; Iverson and Denlinger, 2001; Parsons et al., 2001; de Haas et al., 2015). The collisional, frictional, and viscous forces can be evaluated by considering the simple shear of the granular and fluid phases (Iverson, 1997). As a result, the Bagnold number $N_B$, which describes the ratio of the collisional force to the viscous force, can be calculated as

$$N_B = \frac{\phi_{ft}\rho_p d_p^2 \dot{\gamma}}{(1 - \phi_{ft})\mu_f},$$
(19)

where $\phi_{ft}$ is taken as the spatially averaged local solid volume fraction at the front region. The shear rate is denoted by $\dot{\gamma}$. In the current work, we focus on the propagation of the surge front, so $\dot{\gamma}$ can be calculated as

$$\dot{\gamma} = \frac{v_{ft}}{h_{ft}}.$$
(20)

The Savage number $N_S$ can be used to measure the relative importance of collisional and frictional forces without the consideration of fluid effects.

$$N_S = \frac{\rho_p d_p^2 \dot{\gamma}^2}{(\rho_p - \rho_f)gh_{ft}\tan\theta},$$
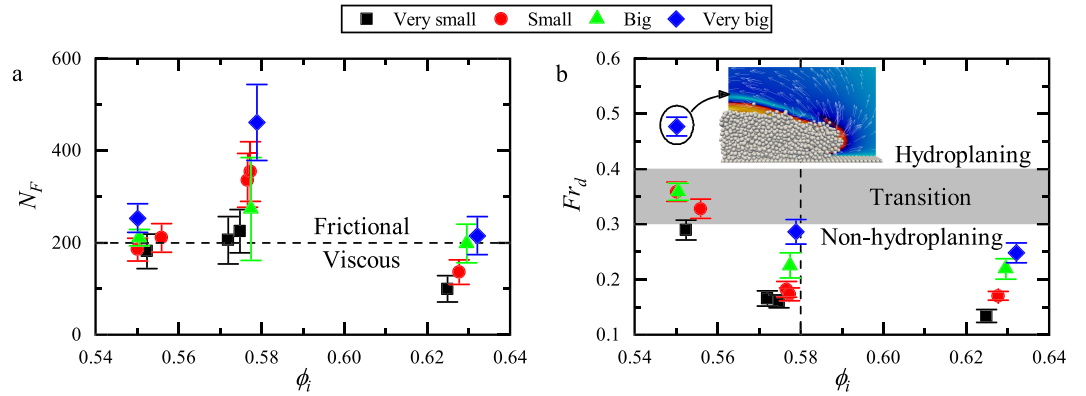(21)

**Figure 13.** Variations of (a) the Friction number, $N_F$, and (b) the densimetric Froude number, $Fr_d$, of immersed granular collapses with different initial packing densities and column sizes. The dashed line in (a) shows the boundary between the friction dominant and viscous force dominant regimes (Parsons et al., 2001). The grey area in (b) shows the critical range of $Fr_d$ for the transition of hydroplaning (Mohrig et al., 1998). The inset in (b) shows the granular front in L-VB during runout.

where $\theta$ is the internal friction angle, which is taken as the inverse tangent of the friction coefficient $\mu$ and is here equal to 21.8°. The Friction number $N_F$ represents the ratio of frictional force to viscous force.

$$N_F = \frac{\phi_{ft}(\rho_p - \rho_f)gh_{ft}\tan\theta}{(1-\phi_{ft})\mu_f\dot{\gamma}}. \tag{22}$$

Previous experimental works have revealed that these three dimensionless numbers are instrumental in determining which force contributes the most to the stoppage of geophysical flows (Iverson, 1997; Parsons et al., 2001). In general, the collisional force starts to dominate over the viscous and frictional forces when $N_B > 200$ and $N_S > 0.1$, respectively (Iverson, 1997). Meanwhile, Parsons et al. (2001) suggested that the frictional force starts to become the dominant resistance for the propagation of surge front when $N_F > 200$.

In addition, a densimetric Froude number $Fr_d$ can be used to describe the necessary condition for hydroplaning as granular particles flowing in a viscous fluid (Mohrig et al., 1998). For the column collapse configurations with 0° bed inclination, $Fr_d$ can be calculated as

$$Fr_d = \frac{v_{ft}}{\sqrt{\left(\frac{\rho_p}{\rho_f} - 1\right)gh_{ft}}}. \tag{23}$$

It is noted that the previously selected front length ($0.4L_i$) and the cutoff porosity (0.8) are rather arbitrary, which may have an influence on the calculated dimensionless numbers. Therefore, a sensitivity analysis is performed by varying the front length $l_{ft}$ from $0.32L_i$ to $0.48L_i$ and the cutoff porosity $n_{cut}$ from 0.6 to 0.8. The average front properties and the resultant dimensionless numbers are summarized in Table 1. First of all, both the Bagnold number $N_B$ and the Savage number $N_S$ are much smaller than the transition thresholds (see Table 1), suggesting that particle collision is not the major source of resistance. Instead, the high viscous damping and severe friction play the major role in the stoppage of particles flowing in a viscous fluid for the immersed cases presented in this study. To reveal the effects of initial packing density on the runout dynamics, flow regime analysis is carried out by plotting the dimensionless numbers ($N_F$ and $Fr_d$) against $\phi_i$ in Figure 13, in which the error bars indicate the standard deviations caused by varying $l_{ft}$ and $n_{cut}$. Note that the results for all very small (VS), small (S), big (B), and very big (VB) immersed cases are presented to indicate the column size effects.

In general, the Friction number $N_F$ increases with the increasing column size, as shown in Figure 13a. Besides, $N_F$ is below or close to the experimental transition value of 200 when $\phi_i$ is large (dense packing) due to the small front thickness $h_{ft}$ and the fairly high shear rate $\dot{\gamma}$. The small front thickness is accompanied with reduced confinement and thus weak frictional forces. On the other hand, the high shear rate contributes to a substantial effect from viscous forces. As $\phi_i$ reduces to a medium dense value ($\phi_i \approx 0.58$), the front thickness $h_{ft}$ increases significantly with a limited amount of increase in the front velocity $v_{ft}$,

resulting in a much higher Friction number $N_F$. As a result, frictional forces dominate over viscous forces when the column size is large enough. As $\phi_i$ further reduces to a lower value, the front velocity increases; and hence, the shear rate increases significantly. Consequently, viscous effects become more significant, and the Friction number decreases.

Two different regimes can be identified regarding the densimetric Froude number as $\phi_i$ decreases: (1) $Fr_d$ increases *slowly* when $\phi_i > 0.58$ and (2) $Fr_d$ increases *rapidly* when $\phi_i < 0.58$. For all immersed cases considered in this study, their $Fr_d$ numbers are below the critical range when $\phi_i > 0.58$ (see Figure 13b), meaning that hydroplaning is not significant. It is interesting to find in Figure 13b that the immersed granular collapses with a small column size fall into the nonhydroplaning and transition regimes, while a clear difference regarding the hydroplaning behavior is observed in Figure 12 between the dense and loose cases. It means that granular flows with $Fr_d$ below the upper bound of the transition ($Fr_d = 0.4$) also have different levels of hydroplaning (or nonhydroplaning).

In L-VB, the $Fr_d$ number (the leftmost blue diamond symbol in Figure 13b) lies above the transition zone where hydroplaning becomes most likely to take place (Mohrig et al., 1998). In fact, the lift up of surge front, as shown in the inset of Figure13b, can be recognized as a signature of hydroplaning for granular flows in a viscous fluid. According to Mohrig et al. (1998), the granular front in L-VB moves too fast that it cannot displace the viscous fluid from its contact area with the stationary rough bed in time, resulting in a pressurized and wedge-shaped fluid (lubrication layer) separating the front from the bed. The lubrication layer underneath the granular front is able to dramatically reduce the frictional force, especially the apparent bed friction, which promotes a long runout distance.

## 5. Geophysical Significance

The distinct initiation and runout signatures highlighted by our small-scale coupled fluid-particle simulations may have important implications for the complex behaviors of large-scale submarine landslides or even subaerial landslides where the pore pressure is considered as significant (Iverson et al., 2000), which might also be of tremendous benefit to emergency response planning and to the design of mitigation structures in engineering practice. This section quantitatively discusses the influence of packing density on the collapse initiation time and runout distance, and the limitations of the current work.

### 5.1. Collapse Initiation Time

There are different ways to determine the time it takes for the initial flow acceleration, $t_i$. In the experiment of tilting a layer of glass beads, Pailha et al. (2008) measured the velocity of the top surface and took the intersect between the slope of velocity profile at the constant acceleration phase and the time axis as $t_i$. However, due to the transient nature of the column collapse problem, it is not an easy task to well define a characteristic velocity, and its uniform growth rate probably does not exist. In the experiment of immersed granular collapse, Bougouin and Lacaze (2018) defined $t_i$ as the time it takes for the granular front to travel beyond the sluice gate since the gate removal. However, the initial fall of particles at the top-right corner may mask the delay in the dense cases if $t_i$ is based on a fixed small runout length (see Fig. 3).

Therefore, in this study, we choose to determine the collapse initiation time by the runout profiles. As shown in Figure 7, a typical runout behavior can be divided into three phases: acceleration, constant velocity, and deceleration. A linear line can be drawn based on the constant velocity phase (usually with the maximum slope), and its intercept with the time axis is taken as $t_i$ (see Figure 7).

Figure 14 shows the influence of the initial packing density $\phi_i$ on the collapse initiation time $t_i$ of immersed granular collapses with various column sizes. Again, the packing density $\phi_i = 0.58$ sets a clear boundary between the dense (dilative) and loose (contractive) behaviors. As $\phi_i < 0.58$, $t_i$ is extremely small, almost independent of the column size, and the failure is considered as immediate. It suggests that once a loosely packed landslide is triggered, it leaves almost no time for nearby residence to response.

When $\phi_i > 0.58$, $t_i$ increases rapidly as $\phi_i$ increases. This is likely due to the induced larger negative excess pore fluid pressure when the particles are packed in a denser state. Interestingly, it is also found in Figure 14 that the delay of collapse increases as the column size increases (see the rightmost four data points). It is actually expected since the drainage path increases as the column size increases, so the induced negative excess pore fluid pressure takes longer time to dissipate and it can hold the granular column for a longer period. It is worth mentioning that the initial packing densities of the dense cases are not the same due
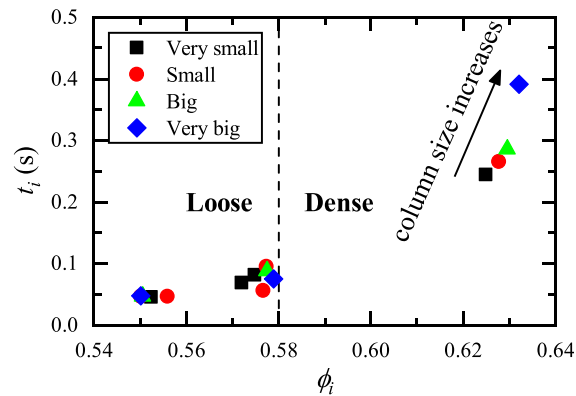
**Figure 14.** Collapse initiation time $t_i$ as a function of the initial packing density $\phi_i$ for different column sizes.

to the randomness in sample generation. Since $t_i$ is expected to be sensitive to $\phi_i$ at the dense state, the dramatic increase of $t_i$ with the column size could be amplified by the increased $\phi_i$ for the larger columns. Note that the scale of the simulated granular collapses is several orders smaller than a field-scale submarine landslide. Therefore, a significant amount of period may be required for the development of a specific event into a destructive flowing mass if the materials are densely packed. This highlights the importance of ground investigation, to determine the in situ packing condition, for emergency response planning.

## 5.2. Size Effect and Runout Scaling

Prediction of the runout distance of geophysical flows has never been an easy task despite its great importance in hazard mitigation works. Previous statistical studies of submarine debris flows suggest power law relationship between the runout distance and the source volume based on the high-quality mapping data from the Storegga area of the western coast of Norway (Issler et al., 2005; Haflidason et al., 2005). Continuum simulations were carried out by Issler et al. (2005), and more recently by Kim et al. (2019), showing that the extremely long runout distances of large submarine landslides can be reproduced with special treatments by invoking hydroplaning or shear wetting. In this regard, the scaling law proposed in the following tries to reflect the influence of hydroplaning on the mobility of granular materials traveling in a viscous fluid.

In this study, we choose the initial height of the granular column ($H_i$) as a representation of its size. Figure 15a plots the normalized runout distance $\tilde{L}_f$ against the normalized height $H_i/d_p$, which shows a power law relationship. The blue and the red dashed lines indicate the lower and upper bounds at the dense and loose limits, respectively. Bougouin and Lacaze (2018) classified the granular flow regimes in a phase diagram with the consideration of column size effects by a dimensionless parameter $(H_i/d_p)^{0.5}$ based on the experiments on dense granular collapses. The exponent 0.5 is close to the lower bound, as shown in Figure 15a. It is clearly shown that the runout distance depends on both the packing density and the column size. Figure 15b shows the effects of the initial packing density on the normalized runout distance. In general, $\tilde{L}_f$ increases as $\phi_i$ decreases, which agrees with the results in Figure 7. The dependence of $\tilde{L}_f$ on both $H_i$ and $\phi_i$ imposes certain difficulties to propose a general scaling law that works across different column sizes and packing densities.

In Section 4, we attribute the long runout distance of the loose cases to hydroplaning, which can be characterized by the densimetric Froude number, $Fr_d$. Comparing Figures 13b and 15b, a similarity can be observed, which implies that there is an intrinsic correlation between the runout distance and $Fr_d$, as shown in Figure 16a. A unique linear relationship correlating $\tilde{L}_f$ and $Fr_d$, independent of the column size and the packing density, can be obtained with the coefficient of determination ($R^2$) as high as 0.9.

The LBM-DEM results and the fitting curve are replotted in Figure 16b in a log–log scale to clearly show both large and small values. In order to test the validity of the $Fr_d$-$\tilde{L}_f$ scaling law, the experimental data from Rondon et al. (2011) are also plotted for comparison. Note that the linear fitting in Figure 16 is merely based on the numerical results. Two experimental cases are considered with one being dense (lower star with $\phi_i = 0.6$) and the other being loose (upper star with $\phi_i = 0.55$). The column length for both experimental cases is $L_i = 6$ cm, and the initial aspect ratio is about 0.67.
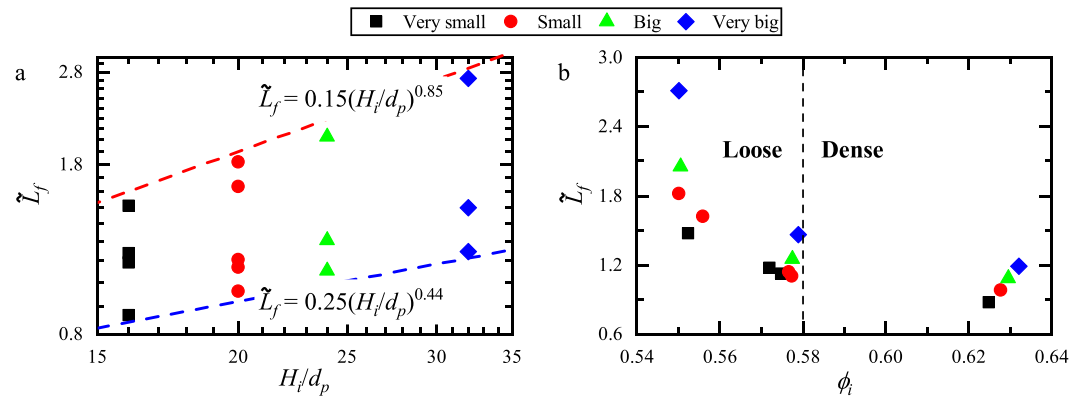
**Figure 15.** Plot of the normalized runout distance $\tilde{L}_f$ against (a) the initial column height $H_i$ normalized by the particle diameter $d_p$ and (b) the initial packing density $\phi_i$.

Since Rondon et al. (2011) did not explicitly report the peak front velocity $v_{ft}$, which is required for the calculation of $Fr_d$, $v_{ft}$ is estimated as the maximum gradient of the $L$-$t$ (plot of front position against time) curve, resulting in 29 and 168 mm/s for the dense and loose cases, respectively. The front thickness $h_{ft}$ is estimated from the granular surface profiles and is taken as 2.37 and 9.35 mm for the dense and loose cases. For the glass beads used in the experiments, their density is the same as our DEM particles, that is, $\rho_p = 2,500$ kg/m$^3$. The fluid is a mixture of water and Ucon oil (less than 18%), whose density was not reported by Rondon et al. (2011) and is approximately taken as $\rho_f = 1,000$ kg/m$^3$. As a result, the estimated $Fr_d$ is 0.153 (0.453), and the calculated $\tilde{L}_f$ is 1.02 (2.53) for the dense (loose) experimental case.

Figure 16b shows that the experimental data follow the fitting curve from the numerical results very well. Generally speaking, for the same column size, a dense packing produces a smaller $Fr_d$ value than a loose packing, leading to a shorter runout distance. It is also worth mentioning that the mean particle size used in the experiments is 225 $\mu$m (Rondon et al., 2011), which is about four times smaller than that in our simulations ($d_p = 1$ mm). On one hand, Figure 16b shows that the linear correlation between $\tilde{L}_f$ and $Fr_d$ is also independent of the particle size. On the other hand, in the experiments, $Fr_d$ is significantly reduced from 0.453 to 0.153 and $\tilde{L}_f$ has more than halved as $\phi_i$ decreases from 0.6 to 0.55. It seems that a small particle size is able to magnify the influence of packing density, resulting in a more dramatic difference between dense and loose runout behaviors. The role of particle size is expected due to its large influence on excess pore fluid pressure generation and dissipation. A smaller particle size is also associated with a smaller Stokes number, which can result in a transition of flow regime and affect the collapse dynamics (Jing et al., 2019). However, the quantification of particle size on the runout of immersed granular flows and the interplay between particle size and packing density require another thorough analysis, which is out of the scope of this study.

It is also of great importance to test the $Fr_d$–$\tilde{L}_f$ scaling law for real submarine landslides. However, the limited field measurement makes the direct comparison between the small-scale granular collapses and the field-scale submarine landslides rather difficult. In particular, a shape correction factor is probably required for the initial geometry, which is not necessary to be rectangular in real cases. Nevertheless, it is still interesting to look at the direct correlation between $Fr_d$ and $\tilde{L}_f$ based on mapped data and back analysis with reasonable estimations.

The field data considered in this study are from Haflidason et al. (2005) and De Blasio et al. (2005) for the well-known Storegga Slide. The approximate values are summarized in Table 2 and explained as below. The release volume $V$ and the landslide width $W$ are taken from De Blasio et al. (2005). Following Issler et al. (2005), the mean cross-sectional area (or release volume per unit width) can be estimated as $A = V/W = 28$ km$^2$. $A$ is considered as a more appropriate measure of the size of a sufficiently wide landslide (compared to the total release volume), which is essentially a two-dimensional plane strain condition. A range from 60 to 100 km is given to the initial length of the landslide, according to the initial profile defined in De Blasio et al. (2005). The runout distance is properly mapped from the field and equal to 410 km (Haflidason et al., 2005). As a result, the calculated normalized runout distance $\tilde{L}_f$ ranges from 3.1 to 5.8.
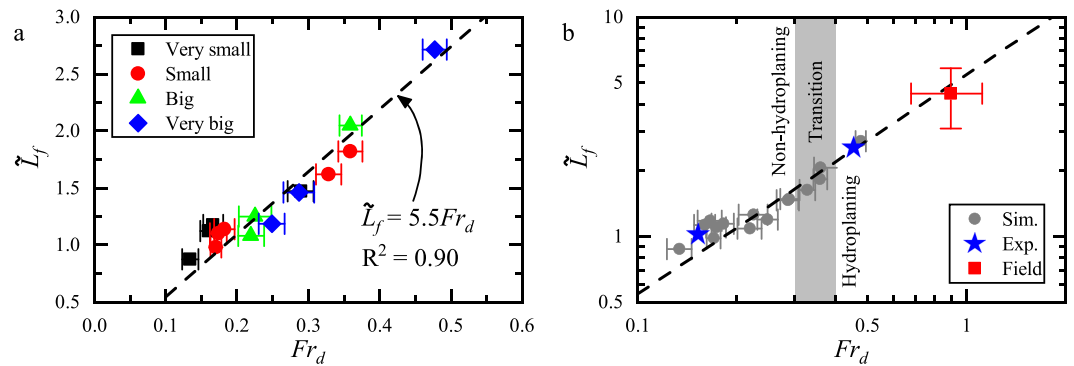
**Figure 16.** (a) Linear correlation between the normalized runout distance $\tilde{L}_f$ and the densimetric Froude number $Fr_d$. The error bars indicate the variations in the calculated $Fr_d$ values. (b) The simulation results and the fitting curve are replotted. The results estimated from the available experimental data (Rondon et al., 2011) are also shown as blue stars for comparison. The red square is the data point for the Storegga Slide estimated from field measurements and back analysis (see Table 2 for the details of calculation).

Løvholt et al. (2017) back analyzed the Storegga Slide using a viscoplastic debris flow model and found that the peak front velocity $v_{ft}$ is between 30 and 35 m/s, which is reached about 1 hr after failure. The front thickness is assigned from 100 to 200 m to show the sensitivity of $Fr_d$ to the estimation. The slope angle (steepness) is measured to be only 1° (Haflidason et al., 2005). Finally, by taking the typical densities of the flowing mass (clay) and the surrounding fluid (water), the resulting $Fr_d$ value ranges between 0.68 and 1.12. It is interesting to see that the estimated $Fr_d$ value locates far beyond the threshold 0.4 (see Figure 16b), meaning that hydroplaning takes place in this particular submarine landslide, which is one of the key mechanisms considered by De Blasio et al. (2005) to accurately capture the runout distance in their simulations.

The result is plotted in Figure 16b with the error bars showing the uncertainties during the estimations of $Fr_d$ and $\tilde{L}_f$. It can be seen that the field data point falls closely onto the extension of the fitting curve derived from small-scale simulations. Nevertheless, there exist several issues that may affect the runout scaling and deserve further attention. The simplified granular collapse configuration differs greatly from real submarine landslides with complex topology and complicated material composition. For example, in the field, the debris may spread laterally due to the lack of confinement in the transverse direction, which may lead to a shorter runout. Besides, there may be a significant amount of clayey soils in the field. When clay is mixed with the surrounding fluid during the flow, a viscoplastic mixture is formed whose behavior is fundamentally different from the granular materials simulated in this study. However, our recent finding shows that

**Table 2**
*Summary of Approximate Values for the Relationship Between the Runout Distance $L_f$ and the Densimetric Froude Number $Fr_d$ for the Large-Scale Storegga Slide and Their Sources*

| Parameters | Values | Sources | Remarks |
|---|---|---|---|
| Release volume, $V$ | 3,100 km³ | De Blasio et al. (2005) | Mapped data |
| Landslide width, $W$ | 110 km | De Blasio et al. (2005) | Mapped data |
| Cross-sectional area, $A$ | 28 km² | Issler et al. (2005) | $A = V/W$ |
| Initial length, $L_i$ | 60–100 km | De Blasio et al. (2005) | Estimated from the initial profile |
| Runout distance, $L_f$ | 410 km | Haflidason et al. (2005) | Mapped data |
| Normalized runout, $\tilde{L}_f$ | 3.1 ~ 5.8 | Calculated | Equation (18) |
| Front velocity, $v_{ft}$ | 30 ~ 35 m/s | Løvholt et al. (2017) | Data from back analysis |
| Front thickness, $h_{ft}$ | 100 ~ 200 m | Løvholt et al. (2017) | Data from back analysis |
| Solid density, $\rho_p$ | 2,000 kg/m³ | Assumed | General property of clay |
| Fluid density, $\rho_f$ | 1,000 kg/m³ | Assumed | General property of water |
| Slope angle, $\theta_b$ | 1° | Haflidason et al. (2005) | Mapped data |
| Froude number, $Fr_d$ | 0.68 ~ 1.12 | Calculated | Equation (23) |

the runout of clay–water mixture in a different context of subaerial flume test scales with the kinetic energy of the flowing mass (Jing et al., 2018), which is well considered by the densimetric Froude number $Fr_d$ (see equation 23) in immersed scenarios. All in all, the close agreement between the granular collapse and the Storegga Slide data implies that the correlation between the runout distance and the densimetric Froude number seems to be universally valid at both small and large scales.

It is worth mentioning that $Fr_d$ is built on a measured parameter, that is, the front velocity $v_{ft}$ instead of the parameters associated with the initial settings. As a result, the $\tilde{L}_f$–$Fr_d$ correlation proposed in this study is regardless of but encoding the initial conditions (i.e., packing density and column size). An alternative approach, within the framework of pore pressure feedback, is to propose a time scale based on the initial parameters, which can quantify the complex interplay between packing density, fluid viscosity, particle and column sizes on flow regime, and runout distance. Such a time scale is expected to be able to characterize the rate and magnitude of pore pressure generation and dissipation.

### 5.3. Limitations of the Current Study

The current study relies on the simplified and miniaturize granular collapse configuration to highlight some key physical processes, with a particular focus on the role of packing density, which may possibly guide the interpretation of field data from submarine landslides. However, there exist many other mechanisms involved in real submarine landslides that deserve further investigations due to the complex material composition and initial and boundary conditions. For example, soils may undergo a series of transitions from failure, through remolding, to a flow phase where mixing with the ambient fluid takes place, continuously changing the properties of the flowing mass (Kim et al., 2019). Besides, the granular collapse assumes an unbalanced initial state, while real submarine landslides may be triggered by small perturbations to a statically balanced initial state. In other words, the granular collapse configuration neglects the triggering process, which may take place in several retrogressive stages and may involve complex shear band propagations (Trapper et al., 2015). In the case of clay-rich sloping materials, failure could be extremely slow and even involve creep mechanisms that may be intrinsically different from the phenomenon observed in section 3.2.

Although the presented LBM-DEM numerical technique is able to accurately capture the fluid-particle interactions at pore-scale resolution, its application in large-scale geophysical flow simulation is still computationally prohibitive. The conclusions we make about the influence of packing density on the collapse initiation time and the runout distance are based on data either from numerical or experimental cases with a constrained small size or field data with rough estimations. In order to draw quantitative conclusions with higher accuracy and reliability, more data should be obtained by directly measuring the kinematics and geometry of active submarine landslides, which poses challenges to the field monitoring technique despite its high cost.

In addition, we limit ourselves to immersed granular flows in the current work. However, it should be noted that some phenomenon observed in a submarine environment might also be prominent in subaerial landslides. For example, shear-induced sediment contraction due to the initially loose packing and the liquefaction of water-saturated sediment at the base are found to be critical for the high speed and long runout distance of the well-known 2014 Oso Landslide (Iverson et al., 2015). For an extension of the current work to subaerial cases, the numerical algorithm should be extended to incorporate a free surface for the LBM fluid (Yang et al., 2018) and its interaction with the DEM particles (Leonardi et al., 2016).

## 6. Concluding Remarks

This paper provides micromechanical insights to the crucial role of initial packing density on the initiation and runout of granular collapses in a viscous fluid, which has never been achieved in previous experimental and numerical studies. To capture the particle kinematics and the induced excess pore fluid pressure accurately, a 3-D coupled LBM-DEM approach is adopted.

Immersed granular collapse is initiated when the downslope driving force (a component of gravity) exceeds the upper limit of resistance (shear strength). The resisting strength of the granular materials is highly dependent on the induced excess pore fluid pressure. LBM-DEM simulations show that the negative excess pore fluid pressure, caused by the dilation of densely packed particles, is capable of enhancing the interparticle contact forces. The strong contact force network can rearrange itself, forming an *arborescent* structure

that prevents the particles from sliding. In the meantime, the granular column only creeps with limited local failures. By contrast, the positive excess pore fluid pressure, caused by the contraction of loosely packed particles, can extensively reduce the interparticle contact forces (static liquefaction). In addition, the contact force chains supporting the loose granular system are vulnerable to buckling, resulting in a catastrophic failure that leads to high-intensity eddies in the fluid field.

For granular collapses with the same column size, the ones in dry condition can gain much higher kinetic energy than the immersed ones. However, it does not mean that the dry granular collapse will always run longer. It is found that the runout distance of immersed granular collapse is heavily dependent on the initial packing density. If the granular column is loosely packed, its runout distance might be even longer than that in the dry counterpart. In order to uncover the reason for the distinct runout behaviors of immersed granular collapse at dense and loose states, flow regime analysis is carried out to identify the relative importance of resistance forces, including collision, friction, and viscous drag. It is found that collision does not play the major role, while friction and viscous drag are the dominant factors to the stoppage of flowing particles. A closer look at the surge front properties reveals that hydroplaning can take place in loose immersed cases, which can be characterized by the densimetric Froude number, $Fr_d$. During hydroplaning, a pressurized fluid is trapped underneath the fast-moving surge front, which can lubricate the contacts between the flowing particles and the rough base and thereby promote a long runout distance.

We finally show that the relationship between the collapse initiation time and the packing density is nonlinear with an abrupt change at $\phi_i = 0.58$. The granular collapse can be considered as immediate when $\phi_i < 0.58$ while $t_i$ increases rapidly as $\phi_i$ increases from 0.58. Besides, regardless of the flow regime (which can be altered by the packing density, column size, and particle size), there exists a unique linear correlation between the normalized runout distance and the densimetric Froude number for immersed granular flows. The strong correlation is confirmed by the available experimental data and the estimated field data for the Storegga Slide. However, in order to generalize the $Fr_d$–$\tilde{L}_f$ scaling to a bigger geophysical flow database, more detailed mapping from the field and reliable back analysis are essential.

Recently, theoretical models of fluid-particle mixtures incorporating the dilatancy effects have been proposed (Iverson and George, 2014; Bouchut et al., 2016; Baumgarten and Kamrin, 2019) and different hypotheses are made regarding the dilatancy model, pore-pressure dissipation, and Darcy's law. Our numerical model has the potential to validate these key hypotheses, as it provides full access to pore-scale information inside the flows. Besides, the influence of packing density on the initiation and runout of immersed granular collapse highlighted by our small-scale LBM-DEM simulations might contribute to a better emergency response plan, risk assessment, and hazard mitigation design for both large-scale submarine and subaerial (where pore pressure plays a role) landslides.

# References

Ai, J., Chen, J.-F., Rotter, J. M., & Ooi, J. Y. (2011). Assessment of rolling resistance models in discrete element simulations. *Powder Technology*, *206*(3), 269–282. https://doi.org/10.1016/j.powtec.2010.09.030

Aidun, C. K., Lu, Y., & Ding, E. J. (1998). Direct analysis of particulate suspensions with inertia using the discrete Boltzmann equation. *Journal of Fluid Mechanics*, *373*, 287–311. https://doi.org/10.1017/S0022112098002493

Balmforth, N. J., & Kerswell, R. R. (2005). Granular collapse in two dimensions. *Journal of Fluid Mechanics*, *538*, 399–428. https://doi.org/10.1017/S0022112005005537

Batchelor, G. (2000). Flow of a Uniform Incompressible Viscous Fluid. In *An Introduction to Fluid Dynamics* (Cambridge Mathematical Library, pp. 174–263). Cambridge: Cambridge University Press. https://doi.org/10.1017/CBO9780511800955.006

Baumgarten, A. S., & Kamrin, K. (2019). A general fluid-sediment mixture model and constitutive theory validated in many flow regimes. *Journal of Fluid Mechanics*, *861*, 721–764. https://doi.org/10.1017/jfm.2018.914

Bhatnagar, P. L., Gross, E. P., & Krook, M. (1954). A model for collision processes in gases. I Small amplitude processes in charged and neutral one-component systems. *Physical Review*, *94*(3), 511–525. https://doi.org/10.1103/PhysRev.94.511

Bouchut, F., Fernández-Nieto, E. D., Mangeney, A., & Narbona-Reina, G. (2016). A two-phase two-layer model for fluidized granular flows with dilatancy effects. *Journal of Fluid Mechanics*, *801*, 166–221. https://doi.org/10.1017/jfm.2016.417

Bougouin, A., & Lacaze, L. (2018). Granular collapse in a fluid: Different flow regimes for an initially dense-packing. *Physical Review Fluids*, *3*(6), 064305. https://doi.org/10.1103/PhysRevFluids.3.064305

Bryn, P., Berg, K., Forsberg, C. F., Solheim, A., & Kvalstad, T. J. (2005). Explaining the storegga slide. *Marine and Petroleum Geology*, *22*(1), 11–19. https://doi.org/10.1016/j.marpetgeo.2004.12.003

Chen, S., & Doolen, G. D. (1998). Lattice Boltzmann method for fluid flows. *Annual Review of Fluid Mechanics*, *30*(1), 329–364. https://doi.org/10.1146/annurev.fluid.30.1.329

Courrech du Pont, S., Gondret, P., Perrin, B., & Rabaud, M. (2003). Granular avalanches in fluids. *Physical Review Letters*, *90*(4), 044301. https://doi.org/10.1103/PhysRevLett.90.044301

Crosta, G. B., Imposimato, S., & Roddeman, D. (2009). Numerical modeling of 2-D granular step collapse on erodible and nonerodible surface. *Journal of Geophysical Research*, *114*, F03020. https://doi.org/10.1029/2008JF001186

Cundall, P. A., & Strack, O. D. L. (1979). A discrete numerical model for granular assemblies. *Géotechnique*, *29*(1), 47–65. https://doi.org/10.1680/geot.1979.29.1.47

De Blasio, F. V., Elverhøi, A., Issler, D., Harbitz, C. B., Bryn, P., & Lien, R. (2005). On the dynamics of subaqueous clay rich gravity mass flows-The giant Storegga Slide, Norway. *Marine and Petroleum Geology*, *22*(1), 179–186. https://doi.org/10.1016/j.marpetgeo.2004.10.014

Delannay, R., Valance, A., Mangeney, A., Roche, O., & Richard, P. (2017). Granular and particle-laden flows: From laboratory experiments to field observations. *Journal of Physics D: Applied Physics*, *50*(5), 053001. https://doi.org/10.1088/1361-6463/50/5/053001

Di Renzo, A., & Di Maio, F. P. (2004). Comparison of contact-force models for the simulation of collisions in DEM-based granular flow codes. *Chemical Engineering Science*, *59*(3), 525–541. https://doi.org/10.1016/j.ces.2003.09.037

Dimakis, P., Elverhøi, A., Høeg, K., Solheim, A., Harbitz, C., Laberg, J. S., et al. (2000). Submarine slope stability on high-latitude glaciated Svalbard-Barents Sea Margin. *Marine Geology*, *162*(2), 303–316. https://doi.org/10.1016/S0025-3227(99)00076-6

de Haas, T., Braat, L., Leuven, J. R. F. W., Lokhorst, I. R., & Kleinhans, M. G. (2015). Effects of debris flow composition on runout, depositional mechanisms, and deposit morphology in laboratory experiments. *Journal of Geophysical Research: Earth Surface*, *120*, 1949–1972. https://doi.org/10.1002/2015JF003525

Haflidason, H., Lien, R., Sejrup, H. P., Forsberg, C. F., & Bryn, P. (2005). The dating and morphometry of the Storegga Slide. *Marine and Petroleum Geology*, *22*(1), 123–136. https://doi.org/10.1016/j.marpetgeo.2004.10.008

Hampton, M. A., Lee, H. J., & Locat, J. (1996). Submarine landslides. *Reviews of Geophysics*, *34*(1), 33–59. https://doi.org/10.1029/95RG03287

Harbitz, C. B., Parker, G., Elverhøi, A., Marr, J. G., Mohrig, D., & Harff, P. A. (2003). Hydroplaning of subaqueous debris flows and glide blocks: Analytical solutions and discussion. *Journal of Geophysical Research: Solid Earth*, *108*(B7), 2349. https://doi.org/10.1029/2001JB001454

He, X., & Luo, L. S. (1997). Lattice Boltzmann model for the incompressible Navier-Stokes equation. *Journal of Statistical Physics*, *88*(3), 927–944. https://doi.org/10.1023/B:JOSS.0000015179.12689.e4

Ilstad, T., Marr, J. G., Elverhøi, A., & Harbitz, C. B. (2004). Laboratory studies of subaqueous debris flows by measurements of pore-fluid pressure and total stress. *Marine Geology*, *213*(1), 403–414. https://doi.org/10.1016/j.margeo.2004.10.016

Issler, D., De Blasio, F. V., Elverhøi, A., Bryn, P., & Lien, R. (2005). Scaling behaviour of clay-rich submarine debris flows. *Marine and Petroleum Geology*, *22*(1), 187–194. https://doi.org/10.1016/j.marpetgeo.2004.10.015

Iverson, R. M. (1997). The physics of debris flows. *Reviews of Geophysics*, *35*(3), 245–296. https://doi.org/10.1029/97RG00426

Iverson, R. M. (2005). Regulation of landslide motion by dilatancy and pore pressure feedback. *Journal of Geophysical Research*, *110*, F02015. https://doi.org/10.1029/2004JF000268

Iverson, R. M., & Denlinger, R. P. (2001). Flow of variably fluidized granular masses across three-dimensional terrain: 1 Coulomb mixture theory. *Journal of Geophysical Research*, *106*(B1), 537–552. https://doi.org/10.1029/2000JB900329

Iverson, R. M., & George, D. L. (2014). A depth-averaged debris-flow model that includes the effects of evolving dilatancy. I. Physical basis. *Proceedings of the Royal Society A: Mathematical, Physical and Engineering Sciences*, *470*(2170), 20130819. https://doi.org/10.1098/rspa.2013.0819

Iverson, R. M., George, D. L., Allstadt, K., Reid, M. E., Collins, B. D., Vallance, J. W., et al. (2015). Landslide mobility and hazards: Implications of the 2014 Oso disaster. *Earth and Planetary Science Letters*, *412*, 197–208. https://doi.org/10.1016/j.epsl.2014.12.020

Iverson, R. M., Reid, M. E., Iverson, N. R., LaHusen, R. G., Logan, M., Mann, J. E., & Brien, D. L. (2000). Acute sensitivity of landslide rates to initial soil porosity. *Science*, *290*(5491), 513–516. https://doi.org/10.1126/science.290.5491.513

Jiang, Y., & Liu, M. (2007). From elasticity to hypoplasticity: Dynamics of granular solids. *Physical Review Letters*, *99*(10), 105501. https://doi.org/10.1103/PhysRevLett.99.105501

Jing, L., Kwok, C. Y., Leung, Y. F., & Sobral, Y. D. (2016a). Extended CFD-DEM for free-surface flow with multi-size granules. *International Journal for Numerical and Analytical Methods in Geomechanics*, *40*(1), 62–79. https://doi.org/10.1002/nag.2387

Jing, L., Kwok, C. Y., Leung, Y. F., & Sobral, Y. D. (2016b). Characterization of base roughness for granular chute flows. *Physical Review E*, *94*(5), 052901. https://doi.org/10.1103/PhysRevE.94.052901

Jing, L., Yang, G. C., Kwok, C. Y., & Sobral, Y. D. (2018). Dynamics and scaling laws of underwater granular collapse with varying aspect ratios. *Physical Review E*, *98*(4), 042901. https://doi.org/10.1103/PhysRevE.98.042901

Jing, L., Yang, G. C., Kwok, C. Y., & Sobral, Y. D. (2019). Flow regimes and dynamic similarity of immersed granular collapse: A CFD-DEM investigation. *Powder Technology*, *345*, 532–543. https://doi.org/10.1016/j.powtec.2019.01.029

Kim, J., Løvholt, F., Issler, D., & Forsberg, C. F. (2019). Landslide material control on tsunami genesis–The Storegga Slide and tsunami (8100 y BP). *Journal of Geophysical Research: Oceans*, *124*, 3607–3627. https://doi.org/10.1029/2018jc014893

Kumar, K., Delenne, J. Y., & Soga, K. (2017). Mechanics of granular column collapse in fluid at varying slope angles. *Journal of Hydrodynamics, Series B*, *29*(4), 529–541. https://doi.org/10.1016/S1001-6058(16)60766-7

Ladd, A. J. C. (1994). Numerical simulations of particulate suspensions via a discretized Boltzmann equation. Part 1 Theoretical foundation. *Journal of Fluid Mechanics*, *271*, 285–309. https://doi.org/10.1017/S0022112094001771

Lagrée, P. Y., Staron, L., & Popinet, S. (2011). The granular column collapse as a continuum: Validity of a two-dimensional Navier-Stokes model with a $\mu$(I)-rheology. *Journal of Fluid Mechanics*, *686*, 378–408. https://doi.org/10.1017/jfm.2011.335

Lajeunesse, E., Monnier, J. B., & Homsy, G. (2005). Granular slumping on a horizontal surface. *Physics of Fluids*, *17*(10), 103,302. https://doi.org/10.1063/1.2087687

Langlois, V. J., Quiquerez, A., & Allemand, P. (2015). Collapse of a two-dimensional brittle granular column: Implications for understanding dynamic rock fragmentation in a landslide. *Journal of Geophysical Research: Earth Surface*, *120*, 1866–1880. https://doi.org/10.1002/2014JF003330

Lee, C.-H., & Huang, Z. (2018). A two-phase flow model for submarine granular flows: With an application to collapse of deeply-submerged granular columns. *Advances in Water Resources*, *115*, 286–300. https://doi.org/10.1016/j.advwatres.2017.12.012

Leonardi, A., Wittel, F. K., Mendoza, M., Vetter, R., & Herrmann, H. J. (2016). Particle-fluid-structure interaction for debris flow impact on flexible barriers. *Computer-Aided Civil and Infrastructure Engineering*, *31*(5), 323–333. https://doi.org/10.1111/mice.12165

Locat, J., & Lee, H. J. (2002). Submarine landslides: Advances and challenges. *Canadian Geotechnical Journal*, *39*(1), 193–212. https://doi.org/10.1139/t01-089

Løvholt, F., Bondevik, S., Laberg, J. S., Kim, J., & Boylan, N. (2017). Some giant submarine landslides do not produce large tsunamis. *Geophysical Research Letters*, *44*, 8463–8472. https://doi.org/10.1002/2017GL074062

Lube, G., Huppert, H. E., Sparks, R. S. J., & Freundt, A. (2005). Collapses of two-dimensional granular columns. *Physical Review E*, *72*(4), 041301. https://doi.org/10.1103/PhysRevE.72.041301

Masson, D. G., Harbitz, C. B., Wynn, R. B., Pedersen, G., & Lovhølt, F. (2006). Submarine landslides: Processes, triggers and hazard prediction. *Philosophical Transactions. Series A, Mathematical, Physical, and Engineering Sciences*, *364*(1845), 2009–2039. https://doi.org/10.1098/rsta.2006.1810

Mohrig, D., Ellis, C., Parker, G., Whipple, K. X., & Hondzo, M. (1998). Hydroplaning of subaqueous debris flows. *GSA Bulletin*, *110*(3), 387–394. https://doi.org/10.1130/0016-7606(1998)110⟨0387:HOSDF⟩2.3.CO;2

Mohrig, D., Elverhøi, A., & Parker, G. (1999). Experiments on the relative mobility of muddy subaqueous and subaerial debris flows, and their capacity to remobilize antecedent deposits. *Marine Geology*, *154*(1), 117–129. https://doi.org/10.1016/S0025-3227(98)00107-8

Mutabaruka, P., Delenne, J.-Y., Soga, K., & Radjaï, F. (2014). Initiation of immersed granular avalanches. *Physical Review E*, *89*(5), 052203. https://doi.org/10.1103/PhysRevE.89.052203

Nisbet, E. G., & Piper, D. J. W. (1998). Giant submarine landslides. *Nature*, *392*, 329–330. https://doi.org/10.1038/32765

Noble, D. R., & Torczynski, J. R. (1998). A Lattice-Boltzmann method for partially saturated computational cells. *International Journal of Modern Physics C*, *09*(08), 1189–1201. https://doi.org/10.1142/s0129183198001084

Owen, D. R. J., Leonardi, C. R., & Feng, Y. T. (2011). An efficient framework for fluid-structure interaction using the lattice Boltzmann method and immersed moving boundaries. *International Journal for Numerical Methods in Engineering*, *87*(1-5), 66–95. https://doi.org/10.1002/nme.2985

Pailha, M., Nicolas, M., & Pouliquen, O. (2008). Initiation of underwater granular avalanches: Influence of the initial volume fraction. *Physics of Fluids*, *20*(11), 111701. https://doi.org/10.1063/1.3013896

Parsons, J. D., Whipple, K. X., & Simoni, A. (2001). Experimental study of the grain-flow, fluid-mud transition in debris flows. *Journal of Geology*, *109*(4), 427. https://doi.org/10.1086/320798

Qian, Y., d'Humières, D., & Lallemand, P. (1992). Lattice BGK models for Navier-Stokes equation. *Europhysics Letters*, *17*(6), 479.

Radjaï, F., Wolf, D. E., Jean, M., & Moreau, J.-J. (1998). Bimodal character of stress transmission in granular packings. *Physical Review Letters*, *80*(1), 61–64. https://doi.org/10.1103/PhysRevLett.80.61

Rondon, L., Pouliquen, O., & Aussillous, P. (2011). Granular collapse in a fluid: Role of the initial volume fraction. *Physics of Fluids*, *23*(7), 073301. https://doi.org/10.1063/1.3594200

Si, P., Shi, H., & Yu, X. (2018). Development of a mathematical model for submarine granular flows. *Physics of Fluids*, *30*(8), 083302. https://doi.org/10.1063/1.5030349

Song, S., Sun, Q., Jin, F., & Zhang, C. (2014). Analysis of parameters in granular solid hydrodynamics for triaxial compression tests. *Acta Mechanica Solida Sinica*, *27*(1), 15–27. https://doi.org/10.1016/S0894-9166(14)60013-6

Staron, L., & Hinch, E. J. (2005). Study of the collapse of granular columns using two-dimensional discrete-grain simulation. *Journal of Fluid Mechanics*, *545*, 1–27.

Topin, V., Monerie, Y., Perales, F., & Radjaï, F. (2012). Collapse dynamics and runout of dense granular materials in a fluid. *Physical Review Letters*, *109*(18), 188001. https://doi.org/10.1103/PhysRevLett.109.188001

Trapper, P. A., Puzrin, A. M., & Germanovich, L. N. (2015). Effects of shear band propagation on early waves generated by initial breakoff of tsunamigenic landslides. *Marine Geology*, *370*, 99–112. https://doi.org/10.1016/j.margeo.2015.10.014

Utili, S., Zhao, T., & Houlsby, G. T. (2015). 3D DEM investigation of granular column collapse: Evaluation of debris motion and its destructive power. *Engineering Geology*, *186*, 3–16. https://doi.org/10.1016/j.enggeo.2014.08.018

Verlet, L. (1967). Computer "experiments" on classical fluids. I Thermodynamical properties of Lennard-Jones molecules. *Physical Review*, *159*(1), 98–103.

Wang, C., Wang, Y., Peng, C., & Meng, X. (2017). Dilatancy and compaction effects on the submerged granular column collapse. *Physics of Fluids*, *29*(10), 103307. https://doi.org/10.1063/1.4986502

Wood, D. (1991). Stress-dilatancy. In *Soil Behaviour and Critical State Soil Mechanics* (pp. 226–255). Cambridge: Cambridge University Press. https://doi.org/10.1017/CBO9781139878272.009

Yang, G. C., Jing, L., Kwok, C. Y., & Sobral, Y. D. (2019). A comprehensive parametric study of LBM-DEM for immersed granular flows. *Computers and Geotechnics*, *114*, 103100. https://doi.org/10.1016/j.compgeo.2019.103100

Yang, G. C., Kwok, C. Y., & Sobral, Y. D. (2018). The effects of bed form roughness on total suspended load via the lattice Boltzmann method. *Applied Mathematical Modelling*, *63*, 591–610. https://doi.org/10.1016/j.apm.2018.07.011

Yu, M.-L., Lee, C.-H., & Huang, Z. (2018). Impulsive waves generated by the collapse of a submerged granular column: A three-phase flow simulation with an emphasis on the effects of initial packing condition. *Journal of Earthquake and Tsunami*, *12*(02), 1840,001. https://doi.org/10.1142/s1793431118400018

Zick, A. A., & Homsy, G. M. (1982). Stokes flow through periodic arrays of spheres. *Journal of Fluid Mechanics*, *115*, 13–26. https://doi.org/10.1017/S0022112082000627

Zou, Q., & He, X. (1997). On pressure and velocity boundary conditions for the lattice Boltzmann BGK model. *Physics of Fluids*, *9*(6), 1591–1598. https://doi.org/10.1063/1.869307